The Astrophysical Journal, 964:189 (21pp), 2024 April 1 https://doi.org/10.3847/1538-4357/ad24ef

A Multiwavelength Study of the Hard and Soft States of MAXI J1820+070 During Its 2018 Outburst

Srimanta Banerjee[1], Gulab C. Dewangan[1], Christian Knigge[2], Maria Georganti[2], Poshak Gandhi[2], N. P. S. Mithun[3], Payaswini Saikia[4,5], Dipankar Bhattacharya[6], David M. Russell[4,5], Fraser Lewis[7,8], and Andrzej A. Zdziarski[9]
[1] Inter-University Centre for Astronomy and Astrophysics (IUCAA), PB No.4, Ganeshkhind, Pune-411007, India; srimanta.banerjee4@gmail.com
[2] School of Physics and Astronomy, University of Southampton, Highfield, Southampton SO17 1BJ, UK
[3] Physical Research Laboratory, Navrangpura, Ahmedabad, Gujarat-380 009, India
[4] Center for Astrophysics and Space Science (CASS), New York University Abu Dhabi, PO Box 129188, Abu Dhabi, UAE
[5] New York University Abu Dhabi, PO Box 129188, Abu Dhabi, United Arab Emirates
[6] Ashoka University, Department of Physics, Sonepat, Haryana, 131029, India
[7] Faulkes Telescope Project, School of Physics and Astronomy, Cardiff University, The Parade, Cardiff, CF24 3AA, Wales, UK
[8] Astrophysics Research Institute, Liverpool John Moores University, 146 Brownlow Hill, Liverpool L3 5RF, UK
[9] Nicolaus Copernicus Astronomical Center, Polish Academy of Sciences, Bartycka 18, PL-00-716 Warszawa, Poland
Received 2023 October 11; revised 2024 January 18; accepted 2024 January 30; published 2024 March 29

Abstract

We present a comprehensive multiwavelength spectral analysis of the black hole (BH) X-ray binary MAXI J1820 +070 during its 2018 outburst, utilizing AstroSat far-UV, soft X-ray, and hard X-ray data, along with (quasi-) simultaneous optical and X-ray data from the Las Cumbres Observatory and NICER, respectively. In the soft state, we detect soft X-ray and UV/optical excess components over and above the intrinsic accretion disk emission ($kT_{\rm in} \sim 0.58$ keV) and a steep X-ray power-law component. The soft X-ray excess is consistent with a high-temperature blackbody ($kT \sim 0.79$ keV), while the UV/optical excess is described by UV emission lines and two low-temperature blackbody components ($kT \sim 3.87$ and $\sim$0.75 eV). Employing continuum spectral fitting, we determine the BH spin parameter ($a = 0.77 \pm 0.21$), using the jet inclination angle of $64^\circ \pm 5^\circ$ and a mass spanning 5–10 $M_\odot$. In the hard state (HS), we observe a significantly enhanced optical/UV excess component, indicating a stronger reprocessed emission in the outer disk. Broadband X-ray spectroscopy in the HS reveals a two-component corona, each associated with its reflection component, in addition to the disk emission ($kT_{\rm in} \sim 0.19$ keV). The softer coronal component dominates the bolometric X-ray luminosity and produces broader relativistic reflection features, while the harder component gets reflected far from the inner disk, yielding narrow reflection features. Furthermore, our analysis in the HS suggests a substantial truncation of the inner disk ($\gtrsim$51 gravitational radii) and a high disk density ($\sim 10^{20}$ cm^{-3}).

Unified Astronomy Thesaurus concepts: Accretion (14); Black hole physics (159); Astronomy data analysis (1858); Low-mass x-ray binary stars (939); X-ray astronomy (1810)

1. Introduction

A low-mass X-ray binary (LMXB) containing a black hole (BH) is a binary stellar system in which the BH accretes matter from a low-mass companion star ($\lesssim 1\ M_\odot$) via the Roche-lobe overflow. Most of the Galactic BH-LMXBs are of a transient nature, spending most of their lifetime in a faint quiescent state. This inactive period is sporadically interrupted by short outbursts (usually lasting for weeks to months), in which the accretion rate increases by several orders of magnitude. During an outburst, a BH-LMXB often evolves through a sequence of different X-ray spectral states: hard state (HS), soft state (SS), and hard/soft intermediate state (HIMS/SIMS; Remillard & McClintock 2006; Belloni 2010), displaying a "q" shaped track in the hardness-intensity diagram (HID; Homan et al. 2001; Homan & Belloni 2005). These spectral states differ in their spectral and timing properties, and are possibly due to a change in the accretion geometry (Belloni & Motta 2016).

A typical outburst of BH-LMXBs generally starts and ends in the HS. The HS X-ray spectrum is dominated by an optically thin component exhibiting roughly a power-law shape (with a photon index of $1.4 < \Gamma < 2.1$), from a few kiloelectronvolts to several hundred kiloelectronvolts, followed by an exponential cutoff (Remillard & McClintock 2006). Although the accretion geometry of the HS is highly debated, this component is thought to arise due to the Compton upscattering of soft seed photons by a hot optically thin electron cloud (*corona*) located somewhere in the vicinity of the compact object (Sunyaev & Titarchuk 1980; Done et al. 2007; Gilfanov 2010; Banerjee et al. 2020). Additionally, there could be a weak contribution to the X-ray spectrum from an optically thick and geometrically thin accretion disk with low temperature, with a typical temperature of $\sim$0.2 keV (Reis et al. 2009; Basak & Zdziarski 2016; Zhang et al. 2020). The lower disk temperature generally suggests that the disk is truncated far from the innermost stable circular orbit (ISCO; Done et al. 2007; Gilfanov 2010; Zdziarski et al. 2021a) (however, for other scenarios, see Reis et al. 2010; Kara et al. 2019). After starting in the HS, a source usually transitions to the SS, and returns to the HS toward the end of the outburst. The SS spectrum is described primarily by a multi-temperature blackbody component originating in the accretion disk (Shakura & Sunyaev 1973), often accompanied by a weak and steep ($\Gamma \geqslant 2.1$) power-law tail extending out beyond 500 keV (Belloni & Motta 2016). The blackbody component typically peaks at $\sim$1 keV, and the disk, contrary to the HS case, reaches

close to the ISCO radius (Done et al. 2007; Gilfanov 2010). While evolving from the HS to the SS (or SS to HS), a BH-LMXB goes through HIMS and SIMS (or SIMS and HIMS) successively. The soft thermal disk component becomes more dominant (accompanied by a decrease in power-law flux) in these intermediate states than the HS.

Apart from the hard Comptonized and soft thermal components, the X-ray spectrum of BH-LMXBs also exhibits reflection features, generated as a fraction of Compton-upscattered photons gets reprocessed in the inner accretion disk. These features mainly include a reflection hump around 20–40 keV, and an iron Kα line around 6.4–6.97 keV that is modified by special and general relativistic effects near the BH (Fabian et al. 1989; Fabian 2005). Besides providing detailed information on the composition and ionization state of the disk, the relativistic X-ray reflection provides a way to determine the spin of the BH and also sheds light on the structure of the corona (García et al. 2013, 2014).

By contrast, with this wealth of data in the X-ray band, the emission in the optical/UV band from these systems is poorly understood. It has been widely accepted that the reprocessing of X-rays in the outer accretion disk is the dominant source of optical/UV emission for BH-LMXBs in the SS (van Paradijs & McClintock 1994). In the HS, the synchrotron emission from the jet can also contribute significantly to the optical/UV band (Russell et al. 2006). Although it is difficult to disentangle the effect of these two components from an individual optical/UV spectrum, theoretical models have predicted that the UV/optical luminosity ($L_{\rm optical/UV}$) is correlated differently with the X-ray luminosity if the emission process is irradiation heating ($L_{\rm optical/UV} \propto L_X^{0.5}$) or radiation from the jet ($L_{\rm optical/UV} \propto L_X^{0.7}$) (Gierliński et al. 2009). However, optical/infrared and X-ray (in the 2–10 keV band) observations of a large sample of X-ray binaries in the HS suggest that both the X-ray reprocessing in the disk and the jet emission show a slope close to 0.6 (holds over from the B to K band) for BH-LMXBs (Russell et al. 2006). Besides, the intrinsic thermal emission (due to viscous heating) from the outer disk may also provide significant optical/UV photons in both states.

The transient LMXB MAXI J1820+070 was discovered with the Monitor of All-Sky X-ray Image (MAXI) on 2018 March 11 (Kawamuro et al. 2018), and 5 days prior in the optical band with the All-Sky Automated Survey for Super-Novae project (Denisenko 2018). Soon after its discovery, X-ray flux and optical G magnitude rose to ∼4 Crab (Shidatsu et al. 2019) and ∼11.2 Crab (Torres et al. 2019), respectively, making it one of the brightest X-ray transients ever observed. The source remained bright and active for several months and underwent re-brightening episodes before fading into quiescence in 2019 February (Russell et al. 2019a). Thanks to its low Galactic interstellar absorption ($N_{\rm H} \sim 1.3 \times 10^{21}$ cm^{-2}, HI4PI Collaboration et al. 2016), and relatively nearby location (2.96 ± 0.33 kpc, Atri et al. 2020), the source has been extensively monitored across several wavelengths: from radio (Bright et al. 2018; Trushkin et al. 2018) to infrared (Casella et al. 2018; Mandal et al. 2018) to optical (Baglio et al. 2018; Bahramian et al. 2018; Gandhi et al. 2018; Littlefield 2018; Sako et al. 2018; Russell et al. 2019a) to X-rays (Homan et al. 2018; Uttley et al. 2018), producing a wealth of information about this accreting system.

The object was dynamically confirmed as a BH with a mass of $M = (5.95 \pm 0.22) M_\odot / \sin^3(i_b)$ (i_b: binary inclination angle) with a K-type companion star (Torres et al. 2020) of mass $0.49 \pm 0.10\, M_\odot$ (Mikołajewska et al. 2022). The binary inclination angle was estimated as $66^\circ < i_b < 81^\circ$ (Torres et al. 2020), although the jet inclination (which is generally assumed to be parallel to the BH spin axis) was found to be $64^\circ \pm 5^\circ$ (Wood et al. 2021). On the other hand, Buisson et al. (2019) found the same to be 30^{+4}_{-5} deg in their reflection analysis with NuSTAR data. However, the detection of X-ray dips confirms that the inclination of the outer disk is indeed high (Kajava et al. 2019).

The source went through all canonical states of BH-LMXBs during the 2018 outburst, following roughly the typical "q" pattern on the HID (Buisson et al. 2019; Chakraborty et al. 2020). It initially stayed in the HS for over 3 months and transitioned to the SS in 2018 July (Homan et al. 2020). A compact jet was observed in the HS (Bright et al. 2018). Also, a strong radio flare associated with the launch of bipolar superluminal ejecta was detected at the beginning of the transition to the SS (Bright et al. 2020). The long-term optical and X-ray monitoring of the source during the outburst phase suggests that the jet contributed significantly to the optical emission in the HS state, while the outer disk emission through irradiation provides the dominant optical flux in the intermediate states and the SS (Shidatsu et al. 2019).

The initial spectral analysis of the HS data implied that two Comptonization components are required to offer a satisfactory fit to the data, and the disk extends close to the ISCO radius (Buisson et al. 2019; Chakraborty et al. 2020). The inclination angle was reported low (∼30°), and iron abundance (approximately five times the solar abundance) was found to be high in these studies. The spectro-timing analysis of Kara et al. (2019) supported their claim related to the extent of the disk. Kara et al. (2019) found out that the corona reduced in spatial extent as the source moves from the HS toward the SS, while the inner disk stays stable roughly at $\sim 2R_g$. On the contrary, the disk was observed to be truncated far from the source in the HS in the spectral analysis of Zdziarski et al. (2021a, 2021b, 2022b) with a two-component corona. Besides, the spectral-timing analysis of De Marco et al. (2021) and Axelsson & Veledina (2021) validate the above observation. Interestingly, the inclination in these works (Zdziarski et al. 2021a, 2022b) was found to be close to the jet inclination angle, and the iron abundance was roughly solar. Finally, the SS observations of this source show an excess emission component in the X-ray spectrum, which was proposed to originate from the plunging region (Fabian et al. 2020). Fabian et al. (2020) also found (using NICER SS data) that the mass of the BH is ∼5–10 $M_\odot$ and the spin lies in the range of 0.5 to −0.5 (for an inclination in the range of 30°–40°). However, Zhao et al. (2021) reported a spin of $a = 0.14 \pm 0.09$ (1σ) using the Insight-HXMT SS data, assuming $M = 8.48^{+0.79}_{-0.72} M_\odot$, inclination $= 63^\circ \pm 3^\circ$, and distance $= 2.96 \pm 0.33$ kpc. Bhargava et al. (2021) studied the characteristic frequencies of several power-density spectral components within the framework of the relativistic precession model, and obtained a spin of $0.799^{+0.016}_{-0.015}$. Thus, there is a discrepancy in the measurement of the spin of this BH.

The multiwavelength spectral analysis of MAXI J1820+070 during its 2018–2019 outburst has only been considered in a few works, e.g., Rodi et al. (2021), Özbey Arabacı et al. (2022), and Echiburú-Trujillo et al. (2024). Rodi et al. (2021) primarily delved into studying the jet properties in the HS on April 12 within the `JetSeT` framework. In contrast, Echiburú-Trujillo

Table 1
Details of AstroSat and NICER Observations Used in This Study

Mission	Obs ID	Instrument	Exposure (ks)	Start Time (UT) (yyyy:mm:dd/hh:mm:ss)	End Time (UT) (yyyy:mm:dd/hh:mm:ss)	State
AstroSat	T02 _ 038T01_900001994	SXT	17.97	2018:03:30/10:45:52	2018:03:31/14:13:04	Hard
	(AstroSat_1994)	LAXPC	37.78	2018:03:30/10:45:51	2018:03:31/14:13:05	⋯
	⋯	CZTI-Quad0	37.17	2018:03:30/10:46:36	2018:03:31/14:13:04	⋯
	⋯	CZTI-Quad1	37.04	”	”	⋯
	⋯	CZTI-Quad2	37.18	”	”	⋯
	⋯	CZTI-Quad3	34.69	”	”	⋯
	⋯	UVIT/FUV-G1	11.39	2018:03:30/12:02:29	2018:03:31/14:11:17	⋯
NICER	1200120115 (NICER-1)	XTI	3.34	2018:03:30/09:15:40	2018:0:30/11:30:20	Hard
	1200120116 (NICER-2)	XTI	10.71	2018:03:31/08:28:18	2018:03:31/19:33:09	”
AstroSat	T02 _ 066T01_900002324	SXT	7.929	2018:08:25/11:10:10	2018:08:25/16:37:28	Soft
	(AstroSat_2324)	LAXPC	11.5	”	2018:08:25/16:37:29	⋯
	⋯	UVIT/FUV-G1	2.845	2018:08:25/11:18:01	2018:08:25/13:20:09	⋯
	⋯	UVIT/FUV-G2	2.739	2018:08:25/14:32:54	2018:08:25/16:35:03	⋯

et al. (2024) focused on the evolution of jet spectral properties and their connection to accretion flow parameters. On the other hand, Özbey Arabacı et al. (2022) analyzed two multi-wavelength observations (near-infrared to hard X-ray) in the HS using SWIFT, INTEGRAL, SMARTS, and TÜBİTAK National Observatory, with one observation during the outburst decay and the other close to the mini-outburst peak. However, the latter work lacked a detailed reflection analysis of hard X-ray spectra, similar to that of Echiburú-Trujillo et al. (2024), and was constrained by low data quality. In contrast, our work conducts a comprehensive spectral analysis of MAXI J1820 +070 in both HS and SS, leveraging high-quality spectroscopic UV/X-ray data from AstroSat and NICER missions, along with photometric optical data from Las Cumbres Observatory (LCO). Our investigation explores the evolution of spectral parameters related to X-ray emission from the inner disk and UV/optical emission from the outer disk. We study how the emission from the inner accretion flow influences the outer disk and constrains the global geometry of the accretion disk. It should be noted that our work marks the first case where data from all AstroSat instruments are employed for studying a source.

The paper is organized as follows. We describe the observations and data reduction in Section 2. The results from the spectral analysis are presented in Section 3. We summarize and discuss our results in Section 4 and draw conclusions in 5.

2. Observations and Data Reduction

We use the UV, soft X-ray, and hard X-ray data acquired with the first dedicated Indian multiwavelength space observatory AstroSat (Singh et al. 2014). It carries four co-aligned scientific payloads: the Ultraviolet Imaging Telescopes (UVIT; Tandon et al. 2017, 2020), the Soft X-Ray telescope (SXT; Singh et al. 2016, 2017), the Large Area X-ray Proportional Counters (LAXPC; Yadav et al. 2016; Antia et al. 2017), and the Cadmium-Zinc-Telluride Imager (CZTI; Vadawale et al. 2016; Bhalerao et al. 2017). AstroSat observed MAXI J1820 +070 twice during its 2018 outburst. To support our AstroSat observations, we also use (quasi-)simultaneous NICER X-ray and LCO optical data. We list all the observations in Tables 1 and 2, and provide more details below. In this work, we use `Heasoft` version 6.30.1 for data processing and spectral analysis.

To identify the spectral states during our AstroSat observations, we use the daily averaged MAXI light curves in the energy bands of 2.0–4.0, 4.0–20.0, and 2.0–20.0 keV and derive the hardness-time and intensity-time diagrams for MAXI J1820+070, which we show in Figure 1. We define hardness as a ratio between the MAXI count rate in the 4.0–20.0 and 2.0–4.0 keV energy bands. We find that the source was in the HS during the first AstroSat observation in 2018 March (AstroSat_1994) and in the SS during the second observation in 2018 August (AstroSat_2324). We employ all the AstroSat instruments from the far-UV (FUV) to hard X-ray bands (UVIT, SXT, LAXPC, and CZTI) to observe the source in the HS. Additionally, we use data from two nearly simultaneous NICER and one simultaneous LCO observations for the HS observation. The two NICER observations combined cover a slightly longer time period than the AstroSat observation period. For the SS observation, we use data from three AstroSat instruments and one quasi-simultaneous LCO observation. In the following subsections, we briefly describe the instruments used for the observations and the data reduction process.

2.1. AstroSat/SXT

The SXT (Singh et al. 2016, 2017) is equipped with X-ray optics and a CCD camera, and operates in the photon counting mode. It is well suited for medium-resolution spectroscopy (FWHM ∼150 eV at 6 keV) in the 0.5–7 keV band, and is also capable of low-resolution imaging (FWHM ∼2′, HPD ∼11′). We process the level-1 data using the SXT pipeline (AS1SXTLevel2-1.4b) available at the SXT payload operation center (POC) website,[10] and generate level-2 clean event files for individual orbits. For each observation, we merge the orbit-wise clean event files using the Julia SXT event merger tool SXTMerger.jl,[11] We obtain the processed and cleaned level-2 data for a net SXT exposure time of ∼17.97 and ∼7.93 ks for the first and second AstroSat observations.

MAXI J1820+070 was very bright, exceeding the Crab flux in the 2–10 keV band in both the HS and SS, thus causing a severe pile-up in the SXT data. To correct for the pile-up, we first generate the SXT radial profile of a blazar Mrk 421 that is

[10] https://www.tifr.res.in/~astrosat_sxt/sxtpipeline.html
[11] https://github.com/gulabd/SXTMerger.jl

Table 2
Details of LCO Observations Used in This Study

Filter	Wavelength Center (nm)	Wavelength Width (nm)	Exposure (s)	Date (yyyy:mm:dd)	Time (UT) (hh:mm:ss)	State
SDSS-i'	754.5	129	20	2018:03:31	7:32:59	Hard
SDSS-r'	621.5	139	20	⋯	7:37:17	⋯
SDSS-g'	477.0	150	20	⋯	7:34:17	⋯
SDSS-i'	754.5	129	40	2018:08:24	21:16:53	Soft
SDSS-r'	621.5	139	40	⋯	21:22:44	⋯
SDSS-g'	477.0	150	40	⋯	21:18:29	⋯

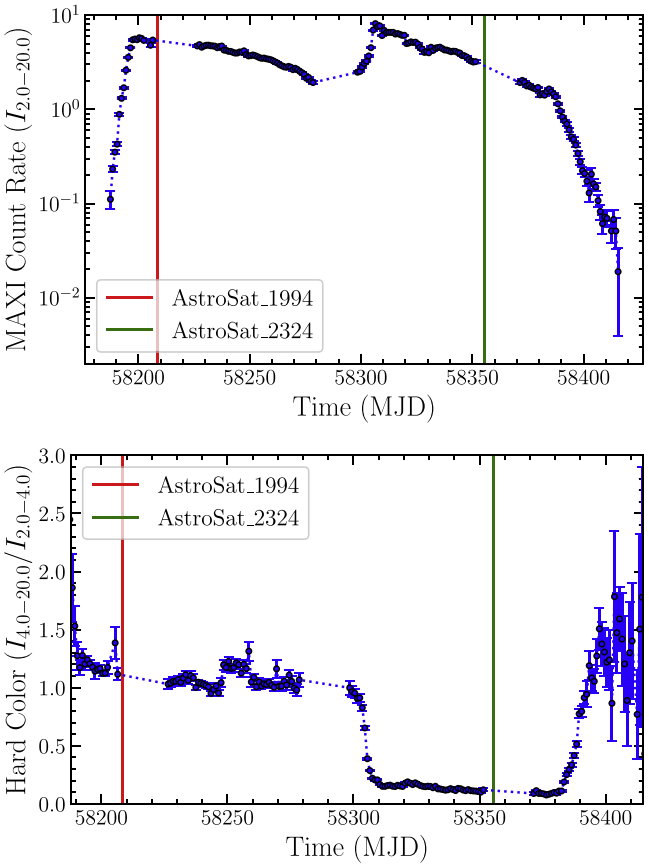

Figure 1. MAXI light-curve in the energy band 2.0–20.0 keV (upper panel), and hardness-time diagram (lower panel) of MAXI J1820+070 during the 2018 outburst. The hardness is defined as the ratio between the MAXI count rate in the 4.0–20.0 and 2.0–4.0 keV energy bands. The two vertical lines on each panel designate the AstroSat observations.

bright but not affected by any pile-up. We then model the radial profile with a Moffat function and a Gaussian profile, and derive the PSF of the SXT as

$$\mathrm{PSF}(r) = A\left(\frac{1}{\left\{1+\left(\frac{r}{r_c}\right)^2\right\}^{1.04}} + 0.08 \times \exp\left\{-\frac{r^2}{2\sigma^2}\right\}\right), \quad (1)$$

with $r_c = 65\farcs3$ and $\sigma = 294\farcs2$. We then fit this PSF with a variable amplitude A to the radial profile of MAXI J1820+070 and obtain the range of radii where the radial profile is well described by the SXT PSF, and the corresponding annular

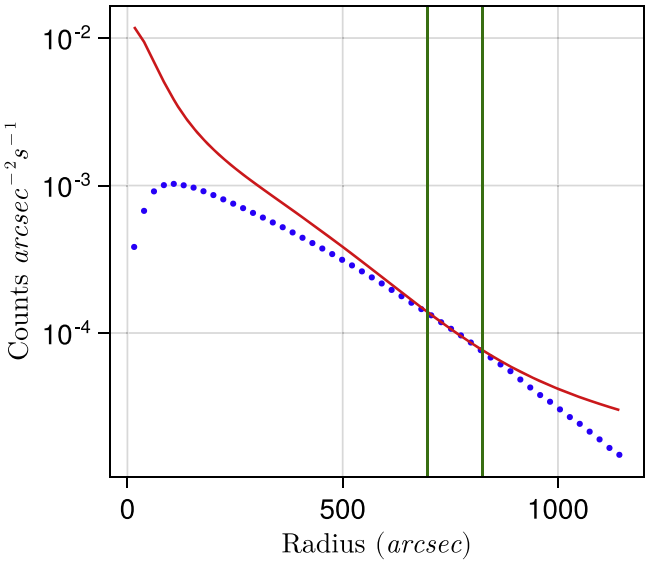

Figure 2. The SXT radial profile of MAXI J1820+070 in the SS (shown in blue dots) compared with the SXT PSF (represented by a red line). The vertical lines mark the inner and outer radii within which the radial profile matches well with the SXT PSF, and is therefore, free of significant pile-up. See Section 2.1 for details.

region is free of pile-up. We find that the annular regions with inner and outer radii of $r_i = 800''$ (194 pixels) and $r_o = 900''$ (218 pixels) for the SS, and $r_i = 618''$ (150 pixels) and $r_o = 907''$ (220 pixels) for the HS are not significantly affected by photon pile-up. In Figure 2, we show the radial profile of MAXI J1820+070 (blue dots) in the SS and the SXT PSF (red line). The vertical lines mark the annular region between r_i and r_o that is free from significant pile-up. The deficit of counts in the outermost regions is caused by the loss of events beyond the detector boundary, due to the off-axis observations and large PSF/HPD of the SXT.

We use the XSELECT tool and extract the source spectrum from the merged level-2 event files using an annular region with r_i and r_o inferred above. Clearly, the ancillary response file (ARF) made available for a circular extraction region centered on the source is inappropriate for a heavily piled-up source like in this case, where a large fraction of counts from the inner region are excluded. Therefore, we derive the corrected ARF as follows. We use the SXT observation of Crab, which is a standard X-ray calibrator. We first extract the SXT spectra of Crab using the same annular regions we used for MAXI J1820+070 in the SS and HS. We fit these Crab spectra with an absorbed power-law model with fixed parameters ($N_{\rm H} = 3.1 \times 10^{21}\,\mathrm{cm}^{-2}$, $\Gamma = 2.1$, $f_X(2-10\,\mathrm{keV}) = 2.4 \times 10^{-8}\,\mathrm{erg\,cm^{-2}\,s^{-1}}$; see Weisskopf et al. 2010) using the

ARF/RMF provided by the SXT POC, and derive the data-to-model ratio. Using these ratios, we correct the ARF and derive separate ARFs appropriate for the SS and HS. As a cross check, we used the corrected ARFs, fit the Crab spectra, and obtained spectral parameters similar to those already known.

2.2. AstroSat/LAXPC

The X-ray instrument LAXPC consists of three proportional counters (LAXPC10, LAXPC20, and LAXPC30) operating in the energy range of 3–80 keV with a temporal resolution of 10 μs (Antia et al. 2017). Out of these three detectors, LAXPC10 has been showing unpredictable high-voltage variations since 2018 March, and LAXPC30 was switched off due to a gas leakage (Antia et al. 2021). Thus, we only use data acquired with the detector LAXPC20 in this work. We extract the LAXPC source and background light curves using the software `laxpcsoftv3.4.3`.[12] The response files `lx20v1.0.rmf` and `lx20cshm01v1.0.rmf` are used for the hard and soft observations, respectively. We group the LAXPC spectra using the FTOOLS package `ftgrouppha` to have a signal-to-noise ratio of at least 25 per bin.

2.3. AstroSat/CZTI

CZTI is a hard X-ray instrument onboard AstroSat providing spectroscopic observations in 22–200 keV energy range and indirect imaging by employing a coded aperture mask (Bhalerao et al. 2017). CZTI consists of four independent quadrants each having an array of 16 CZT detectors and data are available for each quadrant separately. For the analysis of CZTI data, we use CZTI data analysis pipeline version 3.0 along with the associated CALDB.[13] Following the standard pipeline procedure, a clean event list is filtered out from the raw event file. From the clean event files, background subtracted source spectra for each quadrant along with associated response matrices are obtained by using the `cztbin`data task of the data analysis pipeline, which employs the mask-weighting technique. We use the optimal binning scheme of Kaastra & Bleeker (2016) to group the CZTI spectra with a minimum of 25 counts per bin.

2.4. AstroSat/UVIT

UVIT (Tandon et al. 2017, 2020) consists of three channels providing sensitivity in three different bands—FUV (1200–1800 Å) channel, near-UV (NUV; 2000–3000 Å) channel, and the visible (VIS; 3200–5500 Å) channel bands. The FUV and NUV channels are used for scientific observations, while the VIS channel is mainly used for tracking satellite pointing. Both the FUV and NUV channels are equipped with a number of broadband filters for imaging with a point-spread function (PSF) in the range of 1″–1.″5 and slit-less gratings for low-resolution spectroscopy. The FUV channel has two slit-less gratings, FUV-Grating1 and FUV-Grating2 (hereafter, FUV-G1 and FUV-G2), that are arranged orthogonal to each other to avoid possible contamination along the dispersion direction, due to the presence of neighboring sources in the dispersed image. These two channels operate in the photon counting mode. More details on the performance and calibration of the UVIT gratings can be found in Dewangan (2021).

We obtain the level-1 data on MAXI J1820+070 from the AstroSat archive,[14] and process them using the CCDLAB pipeline (Postma & Leahy 2017). We generate orbit-wise drift-corrected, dispersed images for each observation. We then align the orbit-wise images and merge them into a single image for each observation. We use the UVITTOOLS.JL[15] package for spectral extraction following the procedures described in Dewangan (2021) and Kumar et al. (2023). We first locate the position of the zeroth order image of the source in the grating images, and then use the centroids, along the spatial direction at each pixel, along the dispersion direction for the −2 order. We use a 50 pixel width along the cross-dispersion direction and extract the one-dimensional count spectra for the FUV gratings in the −2 order. Following a similar procedure, we also extract background count spectra from source-free regions, and correct the source spectra for the background contribution. We use an updated version of grating responses which are adjusted to match a simultaneous HS Hubble Space Telescope (HST) spectrum of this source (a detailed analysis of the HST spectrum will be discussed in the forthcoming paper, M. Georganti et. al. 2024, in preparation). These files are thus generated following the procedures described in Dewangan (2021).

2.5. NICER

In this work, we consider two NICER observations, which were quasi-simultaneous with the AstroSat HS observation (see Table 1). The NICER data are reduced and calibrated using the `NICERDAS` 2022-01-17_V009 and `CALDB` version xti20210707. The NICER X-ray Timing Instrument (Gendreau et al. 2016) consists of an array of 56 co-aligned X-ray concentrator optics, each of which is paired with a single-pixel silicon drift detector working in the 0.2–12 keV energy band (with a spectral resolution of ∼85 eV FWHM at 1 keV and ∼137 eV at 6 keV). Although 52 detectors were working at the time of the observation, we excluded data from the detectors numbered 14 and 34 as they sometimes exhibit periods of increased noise. We generate cleaned event files of the NICER observations using the script `nicerl2` (with default criteria) and employ the background estimator `nibackgen3C50` (Remillard et al. 2021) to generate the source and background spectra. The scripts `nicerarf` and `nicerrmf` are used to obtain the ARF and RMF files for all the NICER observations. We further obtain background uncorrected NICER light curves in three energy bands: 2.0–4.0, 4.0–10.0, and 0.6–10.0 keV (with 64 s bin time) to produce the NICER HID (see Figure 3). In our work, the NICER hardness is the ratio between the NICER count rate in the 4.0–10.0 and 2.0–4.0 keV bands. We do not find any significant hardness variation between the two NICER observations (see Figure 3), and also within a single observation. Hence, we consider these two observations entirely in the present work. We group the NICER spectra using the FTOOLS package `ftgrouppha` to a signal-to-noise ratio of at least 50 per bin.

[12] https://www.tifr.res.in/~astrosat_laxpc/LaxpcSoft_v1.0/antia/laxpcsoftv3.4.3_07May2022.tar.gz
[13] http://astrosat-ssc.iucaa.in/cztiData
[14] https://astrobrowse.issdc.gov.in/astro_archive/archive/Home.jsp
[15] https://github.com/gulabd/UVITTools.jl

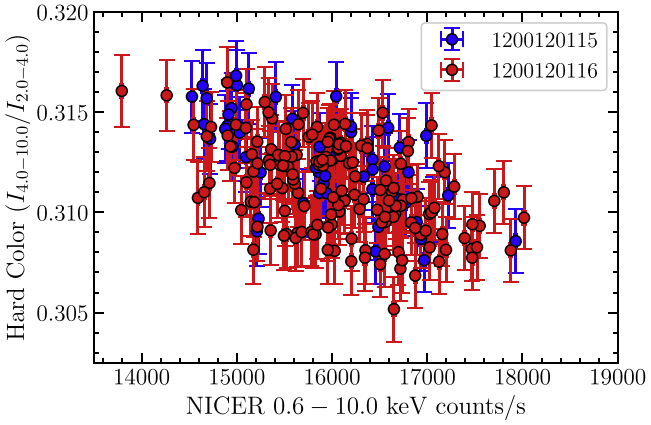

Figure 3. NICER HID for the two observations: 1200120115 and 1200120116. The hardness is defined as the ratio between the NICER count rate in the 2.0–4.0 and 4.0–10.0 keV energy bands.

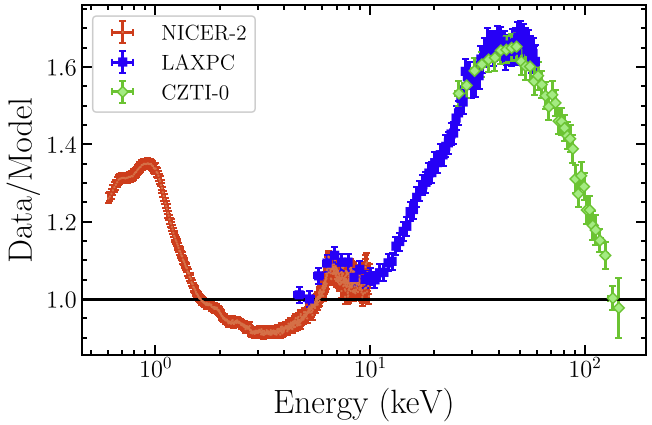

Figure 4. Ratio (data/model) of the 0.6–150.0 keV NICER and AstroSat data to the fiducial model `tbabs *constant *cutoffpl` (HS observation). This exercise is performed just to show different spectral features in the HS spectra. We can clearly see a soft excess, the Fe K-α emission line, and a Compton hump with a peak around ∼40 keV in the HS spectra. Only data from the second NICER observation, LAXPC data, and CZTI Quadrant-0 data are used for this investigation. Data are rebinned for plotting purposes. See Section 3.1.1 for more details.

2.6. LCO

MAXI J1820+070 was monitored during its 2018 outburst in the optical wavelengths by the LCO, as part of an ongoing monitoring campaign of ∼50 low-mass X-ray binaries coordinated by the Faulkes Telescope Project (Lewis 2018). For this study, we use the optical observations obtained with the 1 m robotic telescopes at the LCO nodes of the Cerro Tololo Inter-American Observatory (Chile) and South African Astronomical Observatory, Sutherland (South Africa), which were simultaneous/quasi-simultaneous with the HS and the SS observations of Astrosat, respectively (see Tables 1 and 2). The observations were performed in the Sloan Digital Sky Survey (SDSS) g', i', and r' bands, with 20 s exposure times on each filter for the HS, and 40 s exposure times for the SS. We use the X-ray Binary New Early Warning System data analysis pipeline (Russell et al. 2019b; Pirbhoy et al. 2020) for calibrating the data, computing an astrometric solution for each image using Gaia DR2 positions, performing aperture photometry of all the stars in the image, solving for zero-point calibrations between epochs, and flux calibrating the photometry using the ATLAS All-Sky Stellar Reference Catalog (Tonry et al. 2018).

3. Spectral Analysis

All spectral analyses presented in the following sections are performed using `XSPEC` (Arnaud 1996) version 12.12.1. A multiplicative cross-normalization constant (implemented using `constant` in `XSPEC`) is allowed to vary freely for LAXPC, CZTI, XTI/NICER, and fixed to unity for SXT. We consider an energy range of 6.9–9.5 eV for FUV-G1/FUV-G2, 0.6–7.0 keV for SXT, 4.0–60.0 keV for LAXPC (for the HS observation), 25.0–150.0 keV for CZTI, and 0.6–10.0 keV for XTI/NICER. We limit the LAXPC data to 40 keV for the SS observation as the spectrum is background dominated beyond that. A systematic error of 2% for all the AstroSat instruments (and LCO filters) and 1% for NICER (as suggested by their respective instrument teams) is considered in this work. We apply a gain correction to the SXT data using the `XSPEC` command `gain fit` with the slope fixed to unity. The best-fit offset is found to be ∼0.24 eV for both the HS and SS observations.

We use `tbabs` (Wilms et al. 2000) to take into account the absorption of X-rays in the interstellar medium along the line of sight. We adopt abundances from Wilms et al. (2000) (`wilm` in `XSPEC`), and the photoelectric absorption cross-sections from Verner et al. (1996) (`vern` in `XSPEC`). Furthermore, we assume a distance to the source of 2.96 kpc (Atri et al. 2020). The uncertainties reported in this work correspond to a 90% confidence level for a single parameter of interest.

3.1. HS

3.1.1. X-Ray Spectral Analysis

We begin our investigation with the HS X-ray data in the energy range of 0.6–150.0 keV with an absorbed cutoff power law (i.e., `tbabs*constant*cutoffpl` in `XSPEC` notation). We perform this analysis just to demonstrate different spectral features in the data and consider only the data from the second NICER observation, the LAXPC data, and CZTI Quadrant-0 data for this purpose. We note a soft excess, a broad iron emission line around 6.4 keV, and a Compton hump with a peak at approximately 40 keV in the HS spectra (see Figure 4).

We first fit the broadband continuum of the HS X-ray data (in the energy range of 0.6–150.0 keV) of MAXI J1820+070 with a simple model (Model: `tbabs *constant *(diskbb +nthcomp)`) composed of a `diskbb` (Mitsuda et al. 1984; Makishima et al. 1986) component (for describing the multi-colored blackbody emission from a geometrically thin and optically thick accretion disk), and a thermal Comptonized component `nthcomp` (Zdziarski et al. 1996; Życki et al. 1999) (accounting for the hard coronal emission) in which the soft seed photons are provided by the accretion disk (i.e., `inp_type` of `nthcomp` has been set to 1). The seed photon temperature of `nthcomp` is tied to the inner disk temperature of `diskbb`. This model poorly describes the data (χ^2/dof = 7627.7/2398, where dof stands for degrees of freedom). To obtain a better fit and explore the possibility of another coronal component, we add a second `nthcomp` to the above model (Model: `tbabs*constant*(diskbb +nthcomp(1)+nthcomp(2))`). We tie the seed photon temperature of the two Comptonization components to that of the `diskbb` component. The fit quality improved significantly,

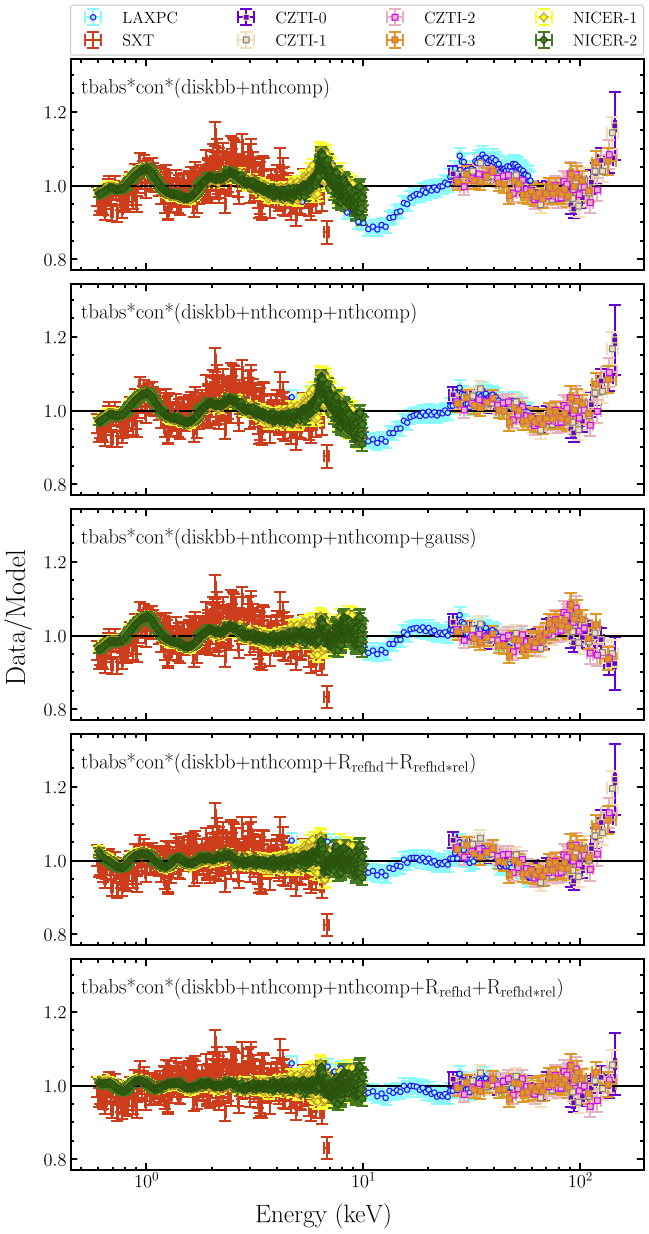

Figure 5. Ratio (data/model) of the 0.6–150.0 keV X-ray multi-instrument (AstroSat+NICER) data to several models for the HS observation. Here, $R_{\rm refhd}$ and $R_{\rm refhd\ *\ rel}$ stand for `reflionxhd` and `relconv*reflionxhd`. In this plot, the model components are mentioned on top of each panel. The panels, from top to bottom, illustrate the improvement in residuals as further model components are added. Data are rebinned for plotting purposes. See Section 3.1.1 for more details.

giving a $\chi^2/{\rm dof} = 7081.3/2395$ (F-test probability of chance improvement of $\sim 10^{-38}$). This improvement is not surprising, as earlier studies have shown (Buisson et al. 2019; Chakraborty et al. 2020; Zdziarski et al. 2021a, 2022b) that the double coronae model offers a better fit to the data. In both these models, the neutral hydrogen column density ($N_{\rm H}$) lies in the range of $1.2–1.4 \times 10^{21}$ atoms cm^{-2}, which is close to the Galactic absorption column along the direction of the source, 1.3×10^{21} atoms cm^{-2} (HI4PI Collaboration et al. 2016). So, hereafter, we will fix $N_{\rm H}$ to the Galactic value for all subsequent spectral analyses performed on the HS observation. The residuals for both these models are depicted in Figure 5. Although the `diskbb` component has already taken care of the soft excess (seen in Figure 4), we still observe significant residuals around 1 keV in both of these models, which could be indicative of a reflection feature (see Figure 5).

However, still, we could not obtain a reasonably good fit, probably due to the strong presence of reflection features (see Figure 4). Thus, we add a Gaussian component to our double Comptonization model to represent the Fe-Kα line observed in the spectra and obtain a huge improvement in the spectral fit (Model: `tbabs *constant *(diskbb+nthcomp(1) +nthcomp(2)+Gauss)`) with χ^2/dof of 3921.7/2392. The residuals around 6.5 keV reduce significantly in this model (see Figure 5). However, the low and high-energy residuals do not improve much. The cross-normalization constant between SXT and LAXPC or CZTI (Quadrant-0/1/2/3) or NICER-1/NICER-2 is found to lie in the range of ∼0.74–0.91 (∼9%–26%), which is within the acceptable limit. The peak energy and width of the iron Kα line come out to be 6.58 ± 0.02 and 0.77 ± 0.02 keV, respectively. The equivalent width corresponding to this line for the NICER data is found to be 0.18 ± 0.33 keV. The inner disk temperature is 0.27 ± 0.05, which is close to the value of ∼0.2 keV obtained earlier for the HS NICER observations (Wang et al. 2020; Dziełak et al. 2021). The two Comptonization components are well separated in power-law indices (Γ) and electron temperatures ($kT_{\rm e}$) in this model, with the best-fit values of them being $\Gamma = 1.72 \pm 0.01$, $kT_{\rm e} = 243.1^{+46.9}_{-65.6}$ and $\Gamma = 1.18 \pm 0.04$, and $kT_{\rm e} = 13.40 \pm 0.69$ keV, respectively. Although adding a Gaussian line to our single Comptonization model provides a huge improvement like the previous case, it still could not produce an acceptable fit (χ^2/d.of = 5507.3/2395). Since other reflection features like the Compton hump are quite prominent in this observation (see Figure 4), we perform an in-depth reflection analysis of joint AstroSat and NICER data.

For a detailed investigation of the broadband spectra and the reflection features, we use a self-consistent reflection model `reflionxhd`, the latest model from the reflection suite `reflionx` (Ross & Fabian 2005, 2007). The `reflionx`-based reflection models generate an angle-averaged reflection spectrum for an optically thick atmosphere (such as the surface of an accretion disk) with constant density irradiated by hard Comptonized emission. This new model `reflionxhd` assumes that the illuminating continuum (responsible for ionizing the disk) is based on the `nthcomp` Comptonization model (as opposed to a cutoff power law), with the soft seed photons being provided by the accretion disk (Jiang et al. 2020; Chakraborty et al. 2021; Connors et al. 2021). Besides, the density of the disk ($n_{\rm e}$) is a model parameter in the range of $15 \leqslant \log(n_e/{\rm cm}^{-3}) \leqslant 22$. We further convolve this component with `relconv` (Dauser et al. 2010), which is part of the `relxill` distribution of models (Dauser et al. 2014; García et al. 2014), to consider the effect of relativistic blurring. We add them to our double Comptonization model to represent the relativistically smeared reflected emission. We tie the power-law index (Γ), electron temperature ($kT_{\rm e}$), and seed photon temperature $kT_{\rm seed}$ of the `reflionxhd` component (i.e., parameters related to the input continuum) with one of our external `nthcomp` components. The ionization parameter (ξ), iron abundance ($A_{\rm Fe}$), and density ($\log(n_{\rm e})$) are left as free parameters. On the other hand, in `relconv`, we fix the spin of the BH (i.e., Kerr parameter) to $a = 0.998$ (i.e., the ISCO radius, $R_{\rm ISCO} = 1.237\,R_g$, where $R_g = GM/c^2$, M is the mass of the BH, G is the Newtonian gravitational constant, and c is the speed

of light in free space) to enable comparisons with previous studies, as this assumption has been made in all the works that performed reflection analysis in the HS (Buisson et al. 2019; Chakraborty et al. 2020; Zdziarski et al. 2021a, 2022b). Since the outer accretion disk could be misaligned with respect to the BH spin axis (Poutanen et al. 2022; Thomas et al. 2022), we assume that the inclination of the inner disk is identical to that of the jet, i.e., $i = 64°$ (Wood et al. 2021), which is presumed to be in the direction of the BH spin axis. We also assume a single emissivity index ($q = q_1 = q_2$), making the break radius (which separates the inner disk with emissivity q_1 from the outer disk with emissivity q_2) redundant, and set the outer disk to $1000R_g$. To account for the narrow core of the Fe-Kα line, we add another `reflionxhd` component to our existing model and tie the parameters of the internal `nthcomp` part (Γ, kT_e, and kT_{seed}) of `reflionxhd` with those of another external `nthcomp` component in our existing model. Additionally, we tie the density and iron abundance of this reflection component to the previously added `reflionxhd`. The density of the disk associated with these two reflection components (relativistic and distant) is perhaps different. However, we tie them to keep our model simple by reducing the number of free parameters. Thus, in the present model (hereafter, referred to as Model 1A), one `nthcomp` (i.e., `nthcomp(1)`) component is reflected through the relativistic reflection component `relconv*reflionxhd(1)`, and another one, i.e., `nthcomp(2)` through the distant reflection component `reflionxhd(2)`. We link the seed photon temperature of these two Comptonization components to the inner disk temperature of the diskbb component. Therefore, the resulting model takes the following form:

- Model 1A: `tbabs * constant * (diskbb + nthcomp(1) +nthcomp(2) + relconv * reflionxhd(1) +reflionxhd(2))`.

We obtain a χ^2/dof of 1904.2/2388, i.e., a huge improvement in the spectral fit compared to our previous models. The results are presented in Table 3 and the residuals are depicted in Figure 5.

We first notice that the residuals below 2 keV and above 10 keV diminish significantly in this model (see Figure 5). The disk temperature, in this case, 0.19 ± 0.01, takes a value almost identical to what was estimated earlier (Wang et al. 2020). Besides, the disk is found to get truncated far from the source, at a distance of $62.3^{+15.2}_{-11.4}$ R_g. We also estimate the inner disk radius from the `diskbb` normalization following the relation:

$$R_{\rm in} = \eta\kappa^2 \sqrt{\frac{N_{\rm disk}}{\cos i}} \frac{D}{10\ {\rm kpc}}, \quad (2)$$

where $R_{\rm in}$ is the true inner radius in kilometers, κ is the spectral hardening factor (i.e., the ratio between the color temperature to effective temperature) (Shimura & Takahara 1995), η is the correction factor for the inner torque-free boundary condition for a Schwarzschild BH ($a = 0$) (Kubota et al. 1998), $N_{\rm disk}$ is the `diskbb` normalization, and D is the distance to the source. However, it is unlikely that the zero torque condition is applicable in the HS, where the disk is truncated far from the ISCO radius. Thus, it is perhaps incorrect to include the correction factor η in our estimation of the true inner radius (see Basak & Zdziarski 2016 for more details). Adopting $\kappa = 1.7$ (Kubota et al. 1998), $i = 64°$, and mass of the BH (M) = 6.75 $M_\odot$ (Mikołajewska et al. 2022), we obtain $R_{\rm in} \sim 73R_g$, which is consistent with the value obtained from the reflection fit.

Table 3
Best-fit Parameter Values and the Corresponding Errors at the 90% Confidence Level for Model 1A (HS)

Spectral Components	Parameters	Model 1A
CONSTANT	$C_{\rm SXT}$	1.0^f
	$C_{\rm LAXPC}$	0.736 ± 0.004
	$C_{\rm CZTI-0}$	0.788 ± 0.007
	$C_{\rm CZTI-1}$	0.796 ± 0.007
	$C_{\rm CZTI-2}$	0.715 ± 0.007
	$C_{\rm CZTI-3}$	0.771 ± 0.007
	$C_{\rm NICER-1}$	0.899 ± 0.002
	$C_{\rm NICER-2}$	0.909 ± 0.002
TBABS	N_H (10^{22} cm^{-2})	0.13^f
DISKBB	$kT_{\rm in}$ (keV)	0.19 ± 0.01
	$N_{\rm disk}$ (10^4)	$32.51^{+1.73}_{-1.56}$
NTHCOMP(1)	Γ	1.59 ± 0.01
	kT_e (keV)	15.39 ± 0.35
	Norm	4.08 ± 0.03
NTHCOMP(2)	Γ	1.17 ± 0.01
	kT_e (keV)	30.55 ± 0.97
	Norm	0.15 ± 0.01
RELCONV*REFLIONXHD(1)	$\mathcal{R}_{\rm in}$ ($R_{\rm ISCO}$)	$50.43^{+12.30}_{-9.18}$
	q	3^f
	i (degree)	64^f
	a	0.998^f
	log(n_e)	20.31 ± 0.03
	ξ	$2365.49^{+64.48}_{-46.93}$
	$A_{\rm Fe}$ ($A_{\rm Fe,solar}$)	1.54 ± 0.04
	Norm	9.14 ± 0.36
REFLIONXHD(2)	ξ	$488.14^{+13.84}_{-12.04}$
	Norm	5.03 ± 0.16
χ^2/dof	...	1904.2/2388

Notes. In XSPEC notation, this model reads as `tbabs *constant *(diskbb +nthcomp(1)+nthcomp(2)+reflionxhd(2)+relconv*reflionxhd(1))`. In this table, f means that the parameter is fixed during the fit and Norm refers to normalization. See Section 3.1.1 for more details.

The power-law index and electron temperature of the two Comptonization components are 1.168 ± 0.002 and $30.55^{+0.95}_{-0.99}$ keV (`nthcomp(2)`), and 1.596 ± 0.003 and 15.39 ± 0.34 keV (`nthcomp(1)`), respectively. The reflecting part of the disk corresponding to the soft Comptonization component is found to be strongly ionized $\xi = 2365^{+64}_{-47}$ compared to that ($\xi = 488^{+14}_{-12}$) illuminated by the hard Comptonization component. Similar two-component Comptonization scenarios with other reflection models (e.g., `relxilllpCp`) were investigated earlier by Buisson et al. (2019), Chakraborty et al. (2020), Zdziarski et al. (2021a, 2022b), and in all these works, it was noted that a double coronae model provides a much better fit to data than a single corona model. The values of the best-fit parameters in Model 1A are consistent with those obtained in an earlier investigation of this source with contemporaneous Insight-HXMT, NuSTAR, and INTEGRAL data (Zdziarski et al. 2022b). Notably, in all the above analyses, constant density reflection models (i.e., n_e is fixed at 10^{15} cm^{-3}) were employed. In some of these works (Buisson et al. 2019; Chakraborty et al. 2020), a higher iron abundance ($>3A_{\rm Fe,solar}$) was reported. In our work, log(n_e) is a variable parameter, and it takes a higher

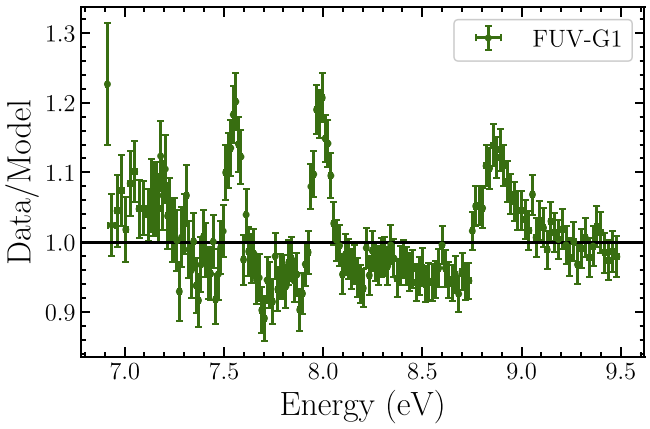

Figure 6. Ratio of the 6.9–9.5 eV FUV-G1 data to the model `redden*bbodyrad` (HS observation). The residuals around 7.55, 8.0, and 8.89 eV are clearly observed. See Section 3.1.2 for more details.

value of 20.32 ± 0.04. Moreover, $A_{\rm Fe}$ is almost close to the solar abundance, which is expected as the secondary star is a weakly evolved low-mass donor star (Mikołajewska et al. 2022). We will discuss the inner disk geometry of the HS in detail in Section 4.1.

In this model (Model 1A), we additionally perform fitting leaving the inclination, and emissivity index as free parameters. However, their values remain unconstrained in their allowed ranges. We also consider a single Comptonization model for performing this reflection study by tying Γ, $kT_{\rm e}$, and $kT_{\rm seed}$ of two `reflionxhd` components with that of a single `nthcomp` component. This model results in a poorer fit, with $\chi^2/{\rm dof} = 2546.3/2391$. Additionally, $kT_{\rm in}$ is found to be quite low $\sim$0.1 keV and the disk is estimated to have almost reached the ISCO radius, $=2.4 \pm 0.3\, R_{\rm ISCO}$, inconsistent with the same calculated from the `diskbb` normalization. Furthermore, we observe significant residuals above 100 keV, which progressively increase with energy (see Figure 5). Therefore, Model 1A not only provides a better statistical description of the data but also yields physically consistent values for all model parameters. We will further consider this model for the multiwavelength spectral analysis of this source in the HS.

3.1.2. UV Spectral Analysis

We fit the FUV-G1 spectrum in the energy range of 6.9–9.5 eV with an absorbed blackbody model (Model: `redden*bbodyrad`) (Meshcheryakov et al. 2018) and obtain a $\chi^2/{\rm dof}$ of 661.6/175. Here, we fix the color excess $E(B-V)$ to 0.17 corresponding to the neutral hydrogen column density of 1.3×10^{21} atoms cm^{-2} along the source line of sight via Equation (15) of Zhu et al. (2017), which is also close to the earlier estimated value of $E(B-V) = 0.163 \pm 0.007$ (Baglio et al. 2018). We clearly observe residuals around 7.55, 8.0, and 8.89 eV (see Figure 6). The residuals around these three energy values most likely correspond to the emission lines: He II λ1640.4, C IV λ1549.1, and Si IV λ1396.8 (Vanden Berk et al. 2001). We add three Gaussian lines (Gaussian in XSPEC notation) to account for these features, and notice that the Gaussian width (σ) of the emission line Si IV is significantly broader than the other lines. The Si IV line is probably a doublet, with components at 1393 and 1403 Å (Morton 2003), which is responsible for making this line broader. Additionally, this feature is sometimes contaminated by or potentially even dominated by a semi-forbidden emission line O IV] λ1402.1 (Vanden Berk et al. 2001). We tie the line widths of He II and C IV lines, and leave that of Si IV as a free parameter. Thus, our new model (hereafter, Model 1B) becomes

•Model 1B: `redden * (Gauss` (He II) + `Gauss` (C IV) +`Gauss` (Si IV) + `bbodyrad(UV))`.

This model provides a $\chi^2/{\rm dof}$ of 222.1/165. The results are presented in Table 4, and the unfolded spectrum and residuals in the form of a ratio (model/data) are depicted in Figure 7.

Table 4
Best-fit Parameter Values and the Corresponding Errors at the 90% Confidence Level for Model 1B (HS)

Spectral Components	Parameters	Values
REDDEN	$E(B-V)$	0.17^{f}
BBODYRAD(UV)	$kT_{\rm uv}$ (eV)	3.27 ± 0.08
	Norm (10^{12})	$2.42^{+0.09}_{-0.02}$
GAUSS (Si IV)	E (eV)	8.90 ± 0.01
	σ (10^{-2} eV)	7.63 ± 1.26
	Norm	0.45 ± 0.05
GAUSS (C IV)	E (eV)	7.99 ± 0.01
	σ (10^{-2} eV)	1.68 ± 0.73
	Norm	0.34 ± 0.04
GAUSS (He II)	E (eV)	7.55 ± 0.01
	σ (10^{-2} eV)	1.68 ± 0.73
	Norm	0.29 ± 0.04
$\chi^2/{\rm dof}$	...	222.1/165

Notes. In `XSPEC`, this model reads as `redden*(Gauss(He II)+Gauss(C IV)+Gauss(Si IV)+bbodyrad(UV))`. In this table, f means that the parameter is fixed during the fit and Norm refers to normalization. The Gaussian width (σ) of the emission lines C IV and He II are tied in this model. The component `bbodyrad` is normalized in the unit of $R^2_{\rm km}/D^2_{\rm 10}$, where $R_{\rm km}$ is the source radius in km. See Section 3.1.2 for more details.

3.1.3. Broadband Optical/UV/X-Ray Spectral Analysis

We will now perform a multiwavelength spectral study of this source in the energy range of 1.64 eV–150 keV and investigate the correlation between the spectral parameters in the X-ray and optical/UV bands. We first add the FUV-G1 spectral data to our X-ray data sets and extrapolate the best-fit X-ray model (Model 1A). We observe a huge UV excess below 0.01 keV (see Figure 8). This indicates that our X-ray model severely underestimates the UV flux, implying the dominance of the effect of irradiation in the outer accretion disk (Gierliński et al. 2009). Thus, we add our best-fit UV model, Model 1B, to the X-ray spectral Model 1A to describe the UV emission in the HS spectra. We set $N_{\rm H} = 0$ for the FUV-G1 spectrum and $E(B-V) = 0$ for the X-ray part of the spectra. Additionally, we fix the Gaussian centroid energies and widths of the emission lines, and the `bbodyrad` temperature in this model to their respective values in Model 1B, and keep only the normalization of these components as free parameters. The parameter `constant` is also kept frozen to unity for the FUV spectrum. Thus, the present model takes the form, `tbabs*redden*constant*(diskbb+nthcomp(1) +nthcomp(2)+reflionxhd +relconv*reflionxhd+ Gauss(He II)+Gauss(C IV) +Gauss(Si IV)+bbodyrad(UV))`. We obtain a $\chi^2/{\rm do.f}$ of 2152.5/2561. Finally, we add LCO data to this setup and find an unacceptable fit with a $\chi^2/{\rm dof}$ of 6543.5/2564. We note

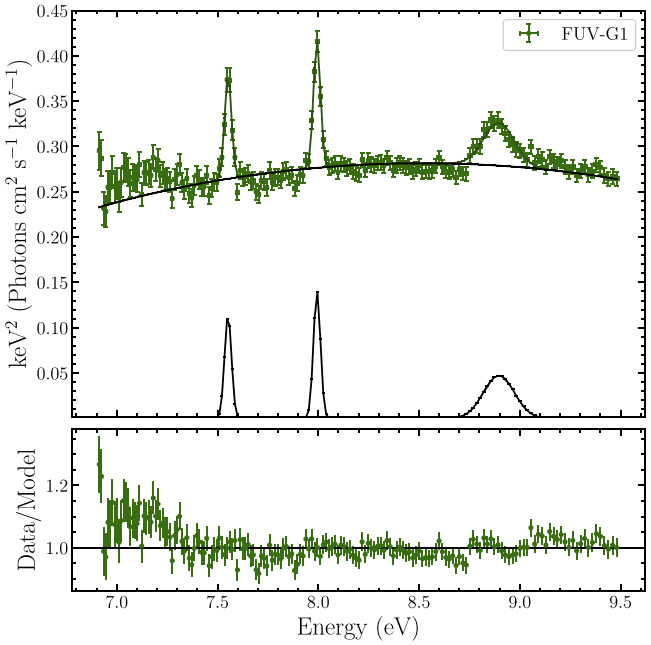

Figure 7. Unfolded spectrum with model (Model 1B) components in black (upper panel) and ratio of the 6.9–9.5 eV FUV-G1 data to Model 1B (lower panel) (HS observation). See Section 3.1.2 for more details.

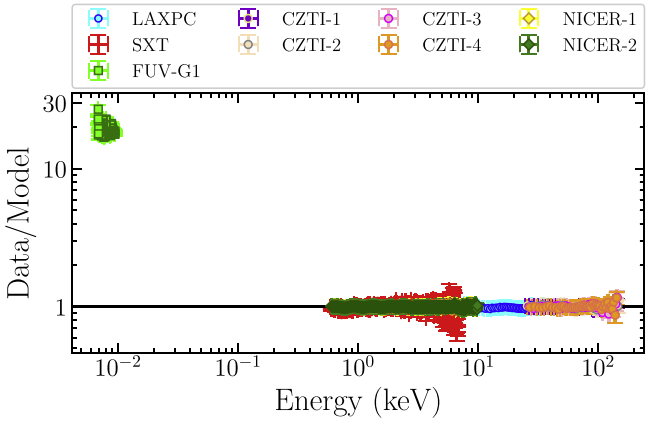

Figure 8. Ratio (data/model) of the 0.0069–150.0 keV multiwavelength (AstroSat+NICER) data to the model: Model 1A (HS observation). We see a huge UV excess below 10 eV. See Section 3.1.3 for more details.

that adding LCO data to our previous model results in significant residuals below 5 eV (see Figure 9). To circumvent the issue, we add another `bbodyrad` component to this model to take care of the excess observed in the mentioned energy band. This results in our model, Model 1C:

•Model 1C: `tbabs * redden * constant * (diskbb +nthcomp(1) + nthcomp(2) + reflionxhd(2) +relconv * reflionxhd(1) + Gauss` (He II) `+Gauss` (C IV) `+ Gauss` (Si IV) `+ bbodyrad(UV) +bbodyrad(optical))`.

We observe a substantial improvement in the spectral fit, $\chi^2/\mathrm{dof} = 2157.7/2562$, and the previously mentioned residuals consequently decrease significantly (see Figure 10). Besides, all the X-ray spectral parameters in this new model take almost

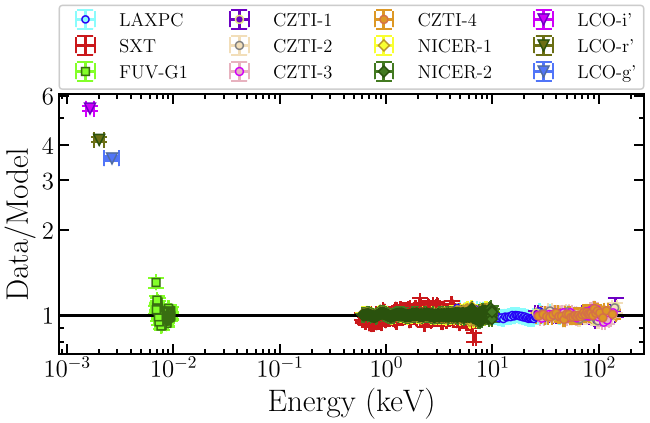

Figure 9. Ratio (data/model) of the 0.00164–150.0 keV multiwavelength (AstroSat+NICER+LCO) data to the combined model: Model 1A + Model 1B (HS observation). We note an optical excess below 5 eV. See Section 3.1.3 for more details.

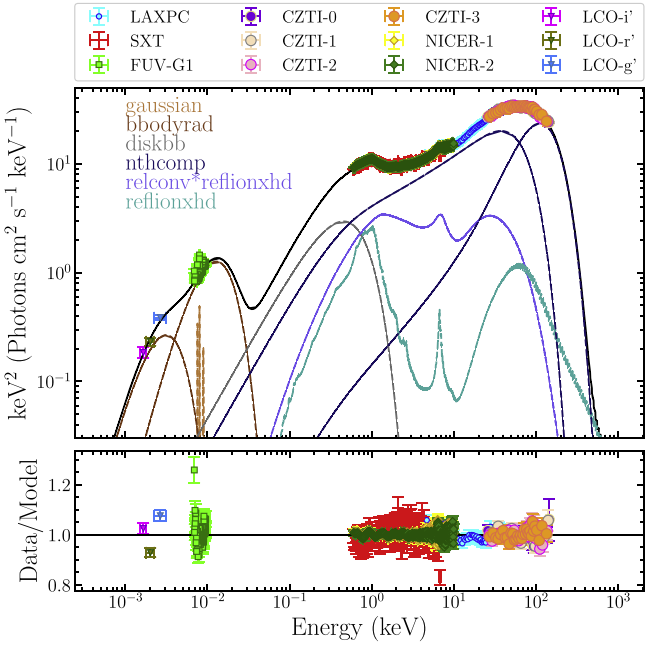

Figure 10. Broadband (optical to hard X-ray) unabsorbed SED (upper panel) and residuals (lower panel), in the form of ratio (data/model), corresponding to Model 1C (HS observation). The total model is represented by a solid black line in the upper panel. Data are rebinned for plotting purposes. See Section 3.1.3 for more details.

identical values to the same parameters of Model 1A, i.e., the previous spectral fit does not get affected due to the inclusion of LCO data. The results are given in Table 5 and the broadband unabsorbed spectral energy distribution (SED) along with residuals is provided in Figure 10. We estimate the reprocessed fraction in this model by taking the ratio of the flux in the 0.5–10.0 eV band (the flux contribution below 0.5 eV is $\lesssim$1%) to that in the 0.1–200.0 keV band, and find this quantity to be $\sim 9 \times 10^{-3}$. Since the outer disk can emit a significant fraction of photons in the 0.5–10.0 eV band through viscous dissipation, we consider only the flux of two `bbodyrad` components and three emission lines in that band for calculating the value of the reprocessed fraction.

Table 5
Best-fit Parameter Values and the Corresponding Errors at the 90% Confidence Level for Model 1C (HS)

Spectral Components	Parameters	Values
CONSTANT	C_{SXT}	1.0^f
	C_{LAXPC}	0.737 ± 0.004
	C_{CZTI-0}	0.789 ± 0.007
	C_{CZTI-1}	0.798 ± 0.007
	C_{CZTI-2}	0.717 ± 0.007
	C_{CZTI-3}	0.772 ± 0.007
	$C_{NICER-1}$	0.899 ± 0.002
	$C_{NICER-2}$	0.909 ± 0.002
REDDEN	$E(B-V)$	0.17^f
TBABS	N_H (10^{22} cm^{-2})	0.13^f
DISKBB	kT_{in} (keV)	0.19 ± 0.01
	N_{disk} (10^5)	3.26 ± 0.18
NTHCOMP(1)	Γ	1.60 ± 0.01
	kT_e (keV)	15.37 ± 0.34
	Norm	4.09 ± 0.08
NTHCOMP(2)	Γ	1.16 ± 0.01
	kT_e (keV)	$30.41^{+0.84}_{+1.18}$
	Norm	0.14 ± 0.02
RELCONV*REFLIONXHD(1)	$\mathcal{R}_{in}$ (R_{ISCO})	$49.39^{+12.48}_{+8.70}$
	i (degree)	64^f
	a	0.998^f
	log(n_e)	20.31 ± 0.02
	ξ	$2358.39^{+391.54}_{-45.02}$
	A_{Fe} ($A_{Fe,solar}$)	1.56 ± 0.04
	Norm	9.21 ± 0.44
REFLIONXHD(2)	ξ	$486.02^{+82.31}_{-09.54}$
	Norm	4.95 ± 0.15
BBODYRAD(UV)	kT_{uv} (eV)	3.27^f
	Norm (10^{11})	$22.30^{+0.15}_{-0.17}$
BBODYRAD(OPTICAL)	$kT_{optical}$ (eV)	0.80 ± 0.03
	Norm (10^{14})	1.31 ± 0.12
GAUSS (Si IV)	Norm	0.49 ± 0.05
GAUSS (C IV)	Norm	0.33 ± 0.04
GAUSS (He II)	Norm	0.26 ± 0.04
Flux (0.1–200.0 keV)	...	18.87
Flux (0.5–10.0 eV)	...	0.18
χ^2/d. o. f	...	2157.7/2562

Notes. In XSPEC, this model reads as: tbabs*redden*constant*(-diskbb+nthcomp(1)+nthcomp(2)+reflionxhd(2)+relconv*-reflionxhd(1) +Gauss(He II)+Gauss(C IV)+Gauss(Si IV) +bbodyrad(UV)+bbodyrad(optical)).In this table, f means that the parameter is fixed during the fit and Norm refers to normalization. All the unabsorbed fluxes are in units of 10^{-8} erg cm^{-2}s^{-1}. In this model, we fix kT_{uv}, the energy and width of emission lines (described by Gaussian line profiles) at their best-fit values as found in Model 1B. See Section 3.1.3 for more details.

3.2. SS

3.2.1. X-Ray Spectral Analysis

We fit the SXT+LAXPC SS spectra in the 0.6–40.0 keV band with a model comprising a multicolored disk blackbody component (diskbb; Mitsuda et al. 1984; Makishima et al. 1986) and a thermal Comptonization component (thcomp; Zdziarski et al. 2020) to describe the weak Comptonization in the SS. We additionally require a single-temperature blackbody component (bbodyrad) to achieve a good fit (F-test probability of chance improvement is $\sim 10^{-90}$). The blackbody component was earlier detected with the NuSTAR data with similar parameters, and proposed to represent the radiation from the plunging region (Fabian et al. 2020). The Comptonization component thcomp is described by three parameters: Γ, kT_e, and covering fraction cov _frac. We convolve this component over diskbb and bbodyrad, as both of them can provide soft seed photons for Comptonization. Thus, we finally arrive at a simple three-component model,

•Model 2A: tbabs*constant*thcomp*(diskbb +bbodyrad).

A similar model was used earlier by Fabian et al. (2020) to describe the broadband SS NuSTAR spectra of this source. In their model, a cutoffpl component was employed to describe the weak Comptonization component, rather than a more physically meaningful thcomp component. Our Model 2A reasonably describes the SS spectrum, yielding a χ^2/do.f of 490.1/413. The best-fit parameters for this model are listed in Table 6. The value of the cross-normalization factor between SXT and LAXPC is found to be 1.21 ± 0.05 ($\sim$20%), which falls within the accepted limit (Antia et al. 2021). We obtain a hydrogen column density (N_H) of $\sim 0.8 \times 10^{21}$ atoms cm^{-2}, which is close to the Galactic column density in the direction of the source, 1.3×10^{21} atoms cm^{-2} (HI4PI Collaboration et al. 2016). The disk (kT_{in}) and blackbody (kT_{BB}) temperatures, and the electron temperature, kT_e (0.58 ± 0.02, 0.79 ± 0.02, and $>$36.5 keV, respectively) are found to be roughly consistent with the nearest (0.64 ± 0.01, 0.92 ± 0.02, and 64.6^{+116}_{-26}, respectively) NuSTAR observation (Fabian et al. 2020) (Observation Nu31 in their paper; the AstroSat observation was performed $\sim$6 days after the Nu31 observation). Furthermore, we find the value of cov_frac $\sim 5 \times 10^{-3}$ to be quite small, implying a very weak Comptonization component. The bbodyrad normalization implies that the X-ray emission is coming from a radius of $\simeq$42–53 km, considering $D = 2.96$ kpc and $\kappa = 1.7$. This region is found to be smaller than the true inner disk radius, $\simeq$88–99 km, as estimated from the diskbb normalization using Equation (2) (we consider $\kappa = 1.7$, $\eta = 0.4$, $i = 64°$ and $D = 2.96$ kpc for this calculation). Since the disk fraction is $\sim$85% (i.e., the fraction of disk flux to the total flux in the 0.1–200.0 keV range) in this observation, the inner disk can be assumed to reach the ISCO radius (McClintock et al. 2014). Therefore, the X-ray emission associated with the bbodyrad component could be related to the radiation coming from the plunging region (Fabian et al. 2020).

We will now replace the diskbb component with a more sophisticated model kerrbb (Li et al. 2005) to describe the emission from a geometrically thin and optically thick accretion disk around a spinning BH (i.e., a Kerr BH). This model takes into account general relativistic effects such as frame-dragging, Doppler boost, gravitational redshift, and bending of light caused by the gravity of a Kerr BH. The spin and mass of the BH, along with the inclination of the inner accretion disk, serve as input parameters for the kerrbb model, in addition to the distance to the source, which we fix at 2.96 kpc, as determined in Atri et al. (2020). In our spectral analysis, we incorporate the effects of both limb-darkening and returning radiation by setting both r_flag and l_flag of kerrbb to 1. In addition, we set the spectral hardening factor to the default

Table 6
Best-fit Parameter Values and the Corresponding Errors at the 90% Confidence Level for Models 2A, 2B, and 2C (SS)

Spectral Components	Parameters	Model 2A	Model 2B		Model 2C
			i (Free)	i (Fixed)	
CONSTANT	C_{SXT}	1.0^{f}	1.0^{f}	1.0^{f}	1.0^{f}
	C_{LAXPC}	1.21 ± 0.05	1.26 ± 0.05	1.25 ± 0.06	1.21 ± 0.06
TBABS	N_H (10^{20} cm^{-2})	$8.03^{+0.98}_{-0.67}$	$11.00^{+0.50}_{-0.87}$	10.34 ± 0.86	$8.07^{+0.92}_{-0.71}$
DISKBB	kT_{in} (keV)	0.58 ± 0.02	...	...	...
	N_{disk} (10^4)	$3.10^{+0.50}_{-0.27}$	...	...	...
BBODYRAD	kT_{BB}	0.79 ± 0.02	0.87 ± 0.04	0.84 ± 0.04	0.79 ± 0.02
	Norm (10^3)	$2.89^{+0.85}_{-0.49}$	$0.90^{+0.64}_{-0.22}$	$1.31^{+1.16}_{-0.53}$	$2.91^{+0.78}_{-0.53}$
THCOMP	Γ	2.19 ± 0.05	2.15 ± 0.04	$2.16^{+0.05}_{-0.11}$	...
	kT_e (keV)	>36.5	>56.2	>17.04	...
	cov_frac (10^{-3})	4.83 ± 0.99	3.90 ± 0.84	4.11 ± 0.98	...
KERRBB	M ($M_\odot$)	...	$9.73^{+2.25}_{-2.52}$	$8.72^{+3.28p}_{-2.82}$	...
	i (degree)	...	$46.83^{+4.68}_{-10.14}$	64^{f}	...
	a	...	$0.998^{+0.000p}_{-0.157}$	$0.85^{+0.10}_{-0.25}$	...
	κ	...	1.7^{f}	1.7^{f}	...
	$\dot{M}$ (10^{17}g s^{-1})	...	$0.45^{+0.36}_{-0.28}$	$0.80^{+11.30}_{-0.68}$	...
	Norm	...	$7.11^{+58.31}_{-3.03}$	$9.79^{+11.07}_{-2.94}$	...
DISKIR	kT_{disk} (keV)	...	...	...	0.58 ± 0.02
	Γ	...	...	...	2.19 ± 0.05
	kT_e (keV)	...	...	...	>41.6
	L_c/L_d (10^{-3})	...	...	...	8.76 ± 0.76
	Norm (10^4)	...	...	...	$3.08^{+0.46}_{-0.29}$
χ^2/d. o. f	...	490.1/413	464.1/410	467.2/411	490.1/413

Notes. In XSPEC notation, these models read as follows, Model 2A: `tbabs *constant * thcomp*(diskbb+bbodyrad)`, Model 2B: `tbabs *constant *thcomp*(kerrbb+bbodyrad)`, and Model 2C: `tbabs*constant*(diskir+bbodyrad)`. In this table, f means that the parameter is fixed during the fit, p denotes that the parameter is pegged at its limit, and Norm refers to normalization. See Section 3.2.1 for more details.

model value of $\kappa = 1.7$. Thus, the new model takes the form,

- Model 2B: `tbabs*constant*thcomp*(kerrbb +bbodyrad)`

Fitting this model to the data gives a χ^2/dof of 464.1/410. The results from the fit are presented in Table 6. The value of N_H ($\sim 1.10 \times 10^{21}$atoms cm^{-2}) is found to be close to that of Model 2A, and the cross-normalization constant is a little higher, 1.25 ± 0.06.

The spin (a) and mass (M) of the BH in this model come out to be >0.84 and $9.73^{+2.25}_{-2.52}$ $M_\odot$, respectively, for an inclination of $46.8^{+4.7}_{-10.1}$. Torres et al. (2020) found that the inclination of the binary (i_b) lies in the range of 66°–81° based on their intermediate-resolution spectroscopic analysis of the optical counterpart of MAXI J1820+070. They also provided a prediction for the BH's mass: $M = (5.95 \pm 0.22) M_\odot / \sin^3 i_b$. For inclinations between 66° and 81°, this relationship yields a mass range of 5.73–8.34 $M_\odot$, which is slightly smaller than our estimated value. Interestingly, there is a significant discrepancy in the measurement of the spin of this BH between several studies. Zhao et al. (2021) performed a continuum spectral analysis of this source in the SS, similar to our approach, but with a different model (`kerrbb2`) and using Insight-HXMT data. They found a slowly rotating BH with a spin of 0.14 ± 0.09 (1σ), assuming a BH mass of 8.48 and an inclination of the inner disk of 63°. Their analysis also indicated that the BH most likely has a prograde spin if $5.73 M_\odot < M < 8.34 M_\odot$ and an inclination in the range of 66°–81°. On the other hand, Bhargava et al. (2021) analyzed the power-density spectra obtained from NICER high cadence observations of the source in the HS, and employed a relativistic precession model to estimate the spin of the BH. Their analysis yielded a spin value of $a = 0.799^{+0.016}_{-0.015}$, which is close to our value. Additionally, our estimation of the inclination angle is significantly lower than the jet inclination angle of $64° \pm 5°$, which is possibly identical to the angle of the BH's spin axis (see Liska et al. 2018 for an alternative scenario).

The values of mass and spin of a BH in the `kerrbb` model strongly depend on the inclination of the inner disk and the distance to the source (McClintock et al. 2014). Therefore, we also perform spectral fitting with Model 2B, with the inclination angle fixed to the jet inclination angle, which could be used as a proxy for the inner disk inclination angle (assuming that the inner disk's angular momentum is aligned with the BH's spin axis; however, for other scenarios, see Banerjee et al. 2019a, 2019b). We obtain a χ^2/dof of 467.2/411. The mass and spin values of this source are found to be greater than $5.9 M_\odot$ and in the range of 0.60–0.95 (See Table 6), respectively, which are quite consistent with earlier measurements (we restrict the upper limit of the BH mass to 12 $M_\odot$ in our spectral fit). Fabian et al. (2020) employed a similar model, using `cutoffpl` instead of `thcomp` to represent the Comptonization component, in their analysis with NuSTAR observations. They fixed the spin (a) and inclination (i) at 0.2 and 34°, respectively, based on the results reported in Buisson et al. (2019). The best-fit temperatures of the blackbody ($kT_{BB} = 0.84 \pm 0.04$ keV) and the Comptonizing corona ($kT_e > 17$ keV) in our model are roughly in agreement with those derived by Fabian et al. (2020) from the nearest NuSTAR observations.

We will finally consider our third model, where we utilize the irradiated disk model diskir (Gierliński et al. 2009) to describe the broadband X-ray continuum. In addition to this, we use the bbodyrad component mentioned earlier. Apart from describing the emissions from a disk and corona (diskir assumes the diskbb and nthcomp routines for this purpose), diskir (has nine parameters) considers the optical/UV emission resulting from the irradiation of the outer disk by the X-ray emission from the inner accretion disk and corona. Furthermore, this model not only describes the reprocessing of X-rays in the outer accretion disk, but also takes into account the illumination of the inner disk by the Compton tail. In essence, this model considers both the irradiation of the inner accretion disk and the outer accretion disk. We fit the following five parameters of diskir (along with the parameters of bbodyrad and tbabs) to the joint SXT-LAXPC data: (1) the temperature of the accretion disk $kT_{\rm disk}$, the normalization (which is identical to the diskbb normalization), power-law index Γ, electron temperature $kT_{\rm e}$, and a ratio of luminosity in the Compton tail to the unilluminated disk $L_{\rm c}/L_{\rm d}$. Since we are exclusively considering the X-ray part of the total spectra, we will keep the outer disk radius ($\log(r_{\rm out}) = \log(R_{\rm out}/R_{\rm in})$ (where $R_{\rm out}$ and $R_{\rm in}$ denote the outer disk and inner disk radii, respectively) and reprocessed fraction ($f_{\rm out}$: the fraction of bolometric X-ray luminosity thermalized in the outer disk) fixed at 4.5 and 0 (i.e., irradiation of the outer disk is turned off), respectively, as these parameters are constrained from the optical/UV spectrum. We additionally freeze the parameters $f_{\rm in}$ (the fraction of the Comptonized luminosity thermalized in the inner disk) and $r_{\rm irr}$ (the radius of the Compton illuminated disk as a fraction of the inner disk radius) to their default values of 0.1 and 1.2, respectively, since they remain unconstrained when left free. Thus, our full model is,

•Model 2C: tbabs * constant * (diskir + bbodyrad)

We obtain a χ^2/dof of 490/413. The resulting best-fitting parameters are given in Table 6. The value of disk and blackbody temperatures, electron temperature, and the power-law index in this model is almost identical to that of Model 2A.

3.2.2. UV Spectral Analysis

From the X-ray spectral fit of the joint SXT+LAXPC data, we find that the hydrogen column density along the source line of sight can be approximated as $\sim 9.0 \times 10^{20}$ atoms cm^{-2}, which is roughly the median value in our estimated range. Hereafter, we will fix $N_{\rm H}$ to the abovementioned value for all subsequent fits in the SS case. This value corresponds to a color excess of $E(B-V) = 0.12$ via Equation (15) of Zhu et al. (2017), which is roughly consistent with the earlier estimated value of $E(B-V) = 0.163 \pm 0.007$ (Baglio et al. 2018).

We fit the FUV-G1 + FUV-G2 spectra with an absorbed single-temperature blackbody (Model: redden*bbodyrad) (Meshcheryakov et al. 2018) and obtain a χ^2/dof of 895/345. We observe large residuals around 7.21, 7.55, 8.0, 8.34, and 8.89 eV (see Figure 11). The residuals around these five energy values most likely correspond to the five emission lines: N IV λ1718.5, He II λ1640.4, C IV λ1549.1, N IV] λ1486.5, and Si IV λ1396.8 (Vanden Berk et al. 2001; Harris et al. 2016). We thus add five Gaussian lines to account for these features, and find that the width of the emission line Si IV is significantly broader than the other lines as also noted earlier for the HS case

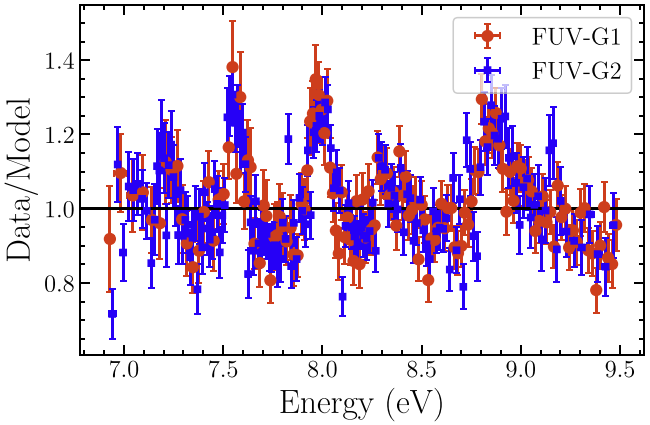

Figure 11. Ratio of the 6.9–9.5 eV FUV-G1 and FUV-G2 data to the model redden*bbodyrad (SS observation). The residuals around 7.21, 7.55, 8.0, 8.34, and 8.89 eV are clearly observed. See Section 3.2.2 for more details.

Table 7
Best-fit Parameter Values and the Corresponding Errors at 90% Confidence Level for Model 2D (SS)

Spectral Components	Parameters	Values
REDDEN	$E(B-V)$	0.12^{f}
BBODYRAD(UV)	$kT_{\rm uv}$ (eV)	3.87 ± 0.24
	Norm (10^{11})	$3.69^{+0.61}_{-0.44}$
GAUSS (Si IV)	E (eV)	8.88 ± 0.02
	σ (10^{-2} eV)	8.52 ± 1.73
	Norm	0.22 ± 0.03
GAUSS (N IV])	E (eV)	8.34 ± 0.02
	σ (10^{-2} eV)	3.19 ± 0.56
	Norm	0.07 ± 0.02
GAUSS (C IV)	E (eV)	7.99 ± 0.01
	σ (10^{-2} eV)	3.19 ± 0.56
	Norm	0.16 ± 0.02
GAUSS (He II)	E (eV)	7.56 ± 0.01
	σ (10^{-2} eV)	3.19 ± 0.56
	Norm	0.13 ± 0.02
GAUSS (N IV)	E (eV)	7.22 ± 0.02
	σ (10^{-2} eV)	3.19 ± 0.56
	Norm	0.08 ± 0.02
χ^2/d. o. f	...	408.6/333

Notes. In XSPEC, this model reads as: redden* (bbodyrad (UV) +Gauss (N IV) +Gauss (He II) +Gauss (C IV) +Gauss (N IV]) +Gauss (Si IV)). In this table, f means that the parameter is fixed during the fit and Norm refers to normalization. The Gaussian width (σ) of the emission lines N IV], C IV, He II, and N IV are tied in this model. See Section 3.2.2 for more details.

(see Section 3.1.2 for a discussion on this). Therefore, we tie the width of the Gaussians corresponding to the lines N IV, He II, C IV, and N IV], but leave that of Si IV as a free parameter. Thus, we arrive at the following model:

•Model 2D: redden * (Gauss (N IV) + Gauss (He II) +Gauss (C IV) + Gauss (N IV]) + Gauss (Si IV) +bbodyrad(UV)).

This model provides a χ^2/dof of 408/333. The results are presented in Table 7, and the unfolded spectrum and residuals in the form of a ratio (model/data) are depicted in Figure 12. The temperature of the blackbody component ($kT_{\rm uv} = 3.87 \pm 0.24$ eV) is found to be slightly higher than the HS case

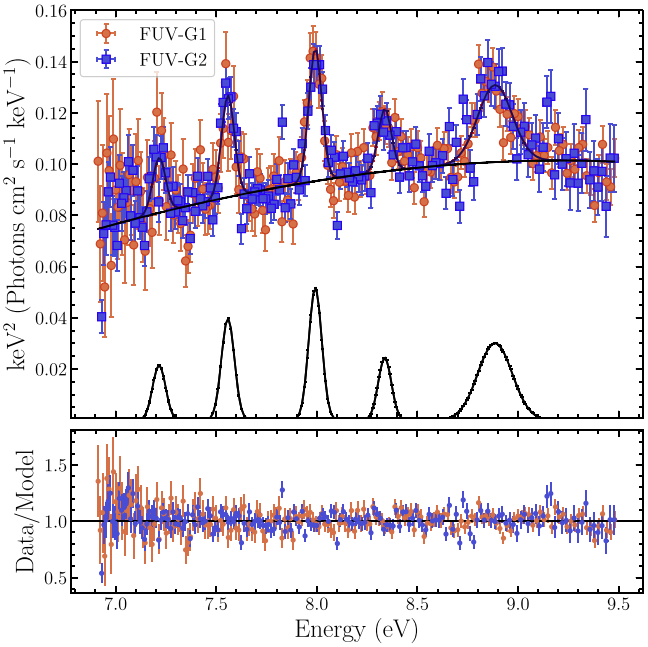

Figure 12. Unfolded spectrum with model (Model 2D) components in black (upper panel) and the ratio of the 6.9–9.5 eV FUV-G1 and FUV-G2 data to Model 2D (lower panel) (SS observation). See Section 3.2.2 for more details.

(=3.27 ± 0.08 eV), although the normalization is an order of magnitude smaller than that of the HS case (i.e., UV flux in the HS is much higher than the SS case).

3.2.3. Broadband Optical/UV/X-Ray Spectral Analysis

We initially add the FUV-G1 and FUV-G2 spectral data sets to our X-ray data sets and extrapolate our best-fit X-ray model (Model 2A) to lower energies, and note a significant UV excess below 10 eV (see Figure 13). However, the UV excess in the SS is considerably weaker than what has been observed in the HS observation. To account for the UV excess, we add our best-fit UV model, Model 2D, to the X-ray model. Thus, we perform a joint UVIT+SXT+LAXPC spectral analysis with the combined model: Model 2A + Model 2D. We set the $N_{\rm H} = 0$ for the UVIT/FUV spectra and $E(B-V) = 0$ for the SXT and LAXPC spectra. Furthermore, we keep all the parameters of Model 2D fixed, except for the normalizations of the individual spectral components. This combined model yields a reasonable fit to the data, with a χ^2/dof of 888.2/755. Now, LCO data are added to this setup, resulting in a fit with χ^2/dof of 1781.9/758. We observed some residuals below 5 eV in the present model (see Figure 14), and add another `bbodyrad` component empirically to take care of the optical excess, as we did previously for the HS case. Our new model thus becomes

•Model 2E: `tbabs * redden * constant * (bbodyrad(UV)` `+Gauss (N IV) + Gauss (He II) + Gauss (C IV)` `+Gauss (N IV]) + Gauss (Si IV) + bbodyrad(optical)` `+thcomp * (diskbb + bbodyrad)`).

We achieve a significant improvement in the spectral fit, obtaining a χ^2/do.f of 900.5/756. Consequently, the residuals below 5 eV are also notably reduced (see Figure 15). The results are given in Table 8. The broadband unabsorbed SED and the residuals are depicted in Figure 15. The temperature ($kT_{\rm optical}$) of the new `bbodyrad` component (=0.75 ± 0.04 eV) is found to

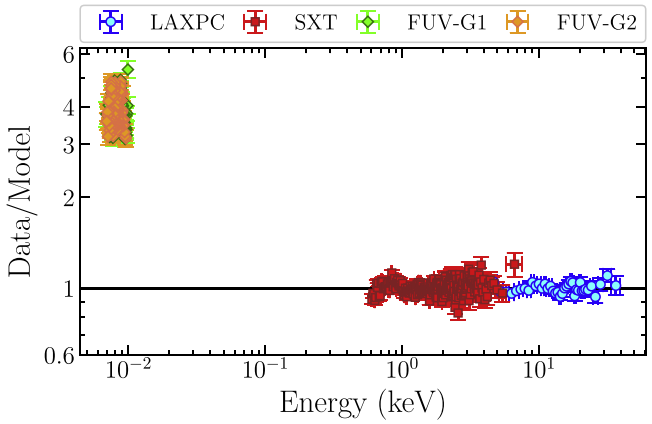

Figure 13. Ratio (data/model) of the 0.00690–40.0 keV multiwavelength AstroSat data to the model: Model 2A (SS observation). We note a UV excess below 10 eV. See Section 3.2.3 for more details.

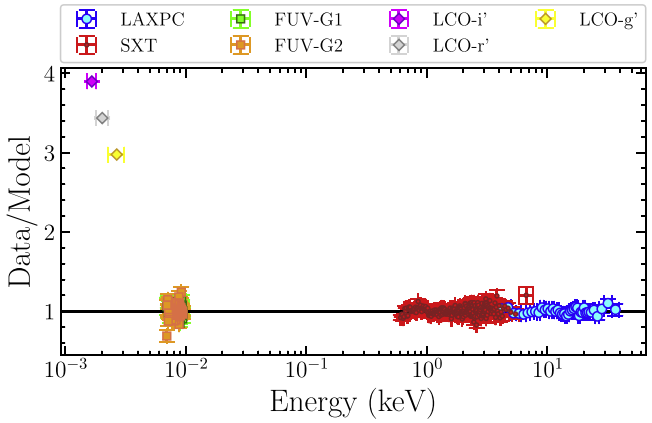

Figure 14. Ratio (data/model) of the 0.00164–40.0 keV multiwavelength (AstroSat+LCO) data to the combined model: Model 2A + Model 2D (SS observation). We see some residuals below 5 eV. See Section 3.2.3 for more details.

be close to the same in the HS case (=0.80 ± 0.03 eV). However, the corresponding normalization is substantially smaller, suggesting a higher optical flux in the HS case. We estimate the reprocessed fraction in this model by taking a ratio of the flux in the 0.5–10.0 eV band (the flux contribution below 0.5 eV is $\lesssim$1%) to the flux in the 0.1–200.0 keV band, and find this quantity to be quite smaller ($\sim 3.5 \times 10^{-3}$) than the HS case. While calculating the flux in the 0.5–10.0 eV band for determining the reprocessed fraction, we do not consider the contribution of the disk (i.e., the `diskbb` flux) since the disk can intrinsically emit a significant fraction of optical/UV photons through viscous dissipation.

Similarly, we add LCO data to the UV/X-ray data, and fit the data with our combined model: Model 2B + Model 2D, and find significant residuals below 5 eV. Therefore, just like the previous case, we consider another `bbodyrad` component to describe the optical excess, and obtain our new model,

•Model 2F: `tbabs * redden * constant * (bbodyrad(UV)` `+Gauss (N IV) + Gauss (He II) + Gauss (C IV)` `+Gauss (N IV]) + Gauss (Si IV) + bbodyrad(optical)` `+thcomp * (kerrbb + bbodyrad)`).

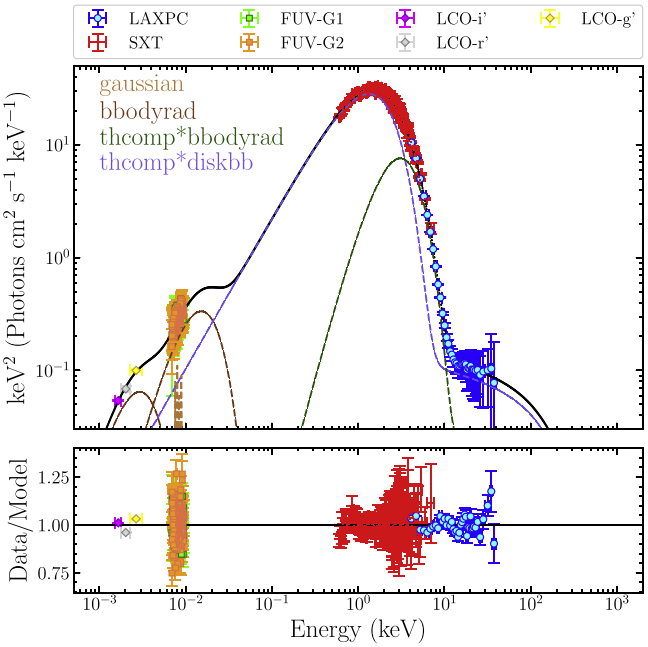

Figure 15. Broadband (optical to hard X-ray) unabsorbed SED (upper panel) and residuals (lower panel), in the form of ratio (data/model), corresponding to Model 2E (SS observation). The total model is represented by a solid black line in the upper panel. Data are rebinned for plotting purposes. See Section 3.2.3 for more details.

We obtain a χ^2/dof of 881.9/756. Similar to the previous case, the residuals below 5 eV are significantly reduced (see Figure 16). The results are presented in Table 8. The broadband unabsorbed SED and the residuals are depicted in Figure 16. In this model, we set the inclination and the mass of the BH to 64° and 6.75 $M_\odot$, respectively. Additionally, we fix the value of the Kerr parameter at $a = 0.75$, which approximately represents the median value within our estimated range for this parameter. Notably, we observe that the spectral parameters in Models 2E and 2F generally exhibit good agreement with each other.

Now, we explore whether the necessity of two blackbody components is a direct consequence of our choice of $E(B-V)$. To investigate this, we leave both the parameters $N_{\rm H}$ and $E(B-V)$ as free parameters in our Model 2E. This results in a slightly worse fit with a χ^2/dof of 893.7/754 and a somewhat lower value of $E(B-V) \approx 0.09$ (the value of $N_{\rm H}$ remains close to its fixed value). However, it is worth noting that the two `bbodyrad` components and the emission lines remain statistically significant. Subsequently, we fix the values of $N_{\rm H}$ and $E(B-V)$ to 0.13×10^{21} atoms cm^{-2} (HI4PI Collaboration et al. 2016) and 0.17, respectively, in our Model 2E, which are the standard values of these quantities in the literature (we consider these values in the HS case). This results in a significantly poorer fit, with a χ^2/dof of 1012.8/756. Nevertheless, both `bbodyrad` components (and the emission lines) remain statistically required to achieve a reasonable fit. In both cases, our statements regarding the SS inner and outer geometry do not change.

Finally, we perform a fit to the LCO+UVIT+SXT+LAXPC data spanning the energy range from 1.64 eV to 40 keV using the combined model: Model 2C + Model 2D. Similar to the previous case, we leave only the normalizations of Model 2D unfrozen, set $E(B-V) = 0$ for the X-ray part, and $N_{\rm H} = 0$ for the optical/UV part of the spectra. Since we are considering optical/UV data here, we keep the parameters $f_{\rm out}$ and $\log(r_{\rm out})$ free during the fitting. In this new model, we exclude the `bbodyrad` component from Model 2D, as the optical/UV continuum is already accounted for by the `diskir` component through the parameters $f_{\rm out}$ and $\log(r_{\rm out})$. Additionally, we find that the emission line N IV becomes statistically insignificant in this model, possibly due to a shift in the UV continuum. So, we remove the Gaussian component corresponding to this line. Therefore, our final model becomes

•Model 2G: `tbabs * redden * constant * (diskir +Gauss` (He II) + `Gauss` (C IV) + `Gauss` (N IV]) +`Gauss` (Si IV) + `bbodyrad`).

This model provides a χ^2/dof of 1230.6/758. The results are given in Table 8, and the unabsorbed SED and residuals are shown in Figure 17. Thus, this model provides a poorer fit to the data compared to the previous phenomenological models, Model 2E and Model 2F.

The value of the reprocessed fraction ($\sim 2 \times 10^{-3}$) obtained from our spectral fit is consistent with that of other BH-LMXBs in the SS (Gierliński et al. 2009). Since the `diskir` normalization is identical to the `diskbb` normalization and $r_{\rm out} = R_{\rm out}/R_{\rm in}$, we can estimate the outer disk radius ($R_{\rm out}$) from the value of $\log(r_{\rm out})$ (=4.38 ± 0.02) using Equation (2) (as $R_{\rm in}$ can be estimated from `diskir` normalization). Adopting $\kappa = 1.7$, $\eta = 0.4$, and $i = 64°$, we find that the size of the disk, $R_{\rm out}$, is (=$2.30 \pm 0.33 \times 10^{11}$) cm. The size of an accretion disk cannot be smaller than the circularization radius due to the conservation of angular momentum, and larger than the tidal truncation radius. To check the consistency of our result, we determine the values of circularization radius ($R_{\rm circ}$) and tidal truncation radius ($R_{\rm tidal}$) using Equations (11) and (12) of Gilfanov & Arefiev (2005), respectively. We find that $R_{\rm circ} \simeq 0.27 R_{\rm orb}$ ($R_{\rm orb}$ is the orbital separation) and $R_{\rm tidal} \simeq 0.57 R_{\rm orb}$, assuming a mass ratio of $q = 0.072$ (Torres et al. 2020). We thus use Kepler's third law of motion to calculate $R_{\rm orb}$, and obtain $R_{\rm orb} \simeq 4.75 \times 10^{11}$ cm, considering an orbital period of 16.45 hr for this binary system (Torres et al. 2020). Therefore, $R_{\rm out}$ lies in between $R_{\rm tidal}$($\simeq 2.71 \times 10^{11}$ cm) and $R_{\rm circ}$($\simeq 1.28 \times 10^{11}$ cm). Torres et al. (2020) approximated the outer disk radius at the time of their observation as $0.6 b_1/R_{\rm orb}$, where b_1 is the distance of the primary from the L_1 point. Using Equation (4.9) of Frank et al. (2002), one finds $b_1/R_{\rm orb} \simeq 0.76 \Rightarrow R_{\rm out} \simeq 2.16 \times 10^{11}$ cm. Hence, our estimated value of the disk size is also consistent with the earlier reported value.

4. Summary of the Main Results and Discussion

During the first AstroSat observation in March 2018, MAXI J1820+070 was in the HS, emitting at an X-ray luminosity (0.1–200.0 keV; hereafter, the total/broadband X-ray flux corresponds to the 0.1–200.0 keV energy range) of $\sim 2 \times 10^{38}$ erg s^{-1} (~23.5% of Eddington luminosity, calculated assuming $M = 6.75\,M_\odot$). Our main results from the multiwavelength spectral analysis of the HS data can be summarized as follows.

1. The HS 0.6–150.0 keV X-ray spectra are found to be composed of two Comptonized emission components with different power-law indices and electron temperatures, their associated reflection components, and a disk component with a temperature of 0.19 ± 0.01 keV (see Section 3.1.1, Figure 10, and Table 3 for more details).

Table 8
Best-fit Parameter Values and the Corresponding Errors at the 90% Confidence Level for Models 2E, 2F, and 2G (SS)

Spectral Components	Parameters	Model 2E	Model 2F	Model 2G
CONSTANT	C_{SXT}	1.0^{f}	1.0^{f}	1.0^{f}
	C_{LAXPC}	1.18 ± 0.05	1.28 ± 0.05	1.18 ± 0.03
TBABS	N_H (10^{20} cm^{-2})	9.0^{f}	9.0^{f}	9.0^{f}
REDDEN	$E(B-V)$	0.12^{f}	0.12^{f}	0.12^{f}
BBODYRAD	kT_{BB}	0.79 ± 0.01	0.89 ± 0.03	0.79 ± 0.01
	Norm (10^3)	$3.41^{+0.57}_{-0.39}$	$0.68^{+0.35}_{-0.28}$	$3.35^{+0.40}_{-0.20}$
DISKBB	kT_{in}	0.56 ± 0.01	...	...
	N_{disk} (10^4)	$3.49^{+0.26}_{-0.18}$	...	...
THCOMP	Γ	2.20 ± 0.05	$2.14^{+0.05}_{-0.15}$	...
	kT_e (keV)	>40.96	>17.42	...
	cov_frac (10^{-3})	5.02 ± 0.92	3.86 ± 1.01	...
KERRBB	M ($M_\odot$)	...	6.75^{f}	...
	i (degree)	...	64^{f}	...
	a	0.75^{f}	...	
	κ	...	1.7^{f}	...
	$\dot{M}$ (10^{17}g s^{-1})	...	$1.48^{+0.13}_{-0.09}$	...
	Norm	...	8.68 ± 0.57	...
DISKIR	kT_{disk} (keV)	...	...	0.57 ± 0.01
	Γ	...	...	2.20 ± 0.04
	kT_e (keV)	...	...	>45.3
	L_c/L_d (10^{-3})	...	...	9.11 ± 0.56
	f_{out} (10^{-3})	...	...	1.98 ± 0.03
	log(r_{out})	...	...	4.38 ± 0.02
	Norm (10^4)	...	...	$3.42^{+0.19}_{-0.10}$
BBODYRAD(UV)	kT_{uv} (eV)	3.87^{f}	3.87^{f}	...
	Norm (10^{11})	$2.55^{+0.04}_{-0.05}$	2.32 ± 0.05	...
BBODYRAD(OPTICAL)	$kT_{optical}$ (eV)	0.75 ± 0.04	0.75 ± 0.04	...
	Norm (10^{13})	$3.51^{+0.55}_{-0.50}$	$3.35^{+0.56}_{-0.50}$	...
GAUSS (Si IV)	Norm	0.25 ± 0.03	0.26 ± 0.03	0.38 ± 0.03
GAUSS (N IV])	Norm	0.09 ± 0.02	0.09 ± 0.02	0.11 ± 0.02
GAUSS (C IV)	Norm	0.18 ± 0.02	0.18 ± 0.02	0.16 ± 0.02
GAUSS (He II)	Norm	0.14 ± 0.02	0.14 ± 0.02	0.09 ± 0.02
GAUSS (N IV)	Norm	0.07 ± 0.03	0.07 ± 0.03	
Flux (0.1–200.0 keV)	...	10.50	11.53	10.56
Flux (0.5–10.0 eV)	...	0.049	0.053	0.056
χ^2/dof	...	900.5/756	881.9/756	1230.6/758

Notes. In XSPEC notation, these models read as follows, Model 2E: `tbabs*redden*con*(bbodyrad(UV)+bbodyrad(optical)+Gauss(N IV)+Gauss(He II)+Gauss(C IV)+Gauss(N IV])+Gauss(Si IV)+thcomp*(bbodyrad+diskbb))`, Model 2F: `tbabs*redden*con*(bbodyrad(UV)+bbodyrad(optical)+Gauss(N IV)+Gauss(He II)+Gauss(C IV)+Gauss(N IV])+Gauss(Si IV)+thcomp*(bbodyrad+kerrbb))`, and Model 2G: `tbabs*redden*con*(Gauss(He II)+Gauss(C IV)+Gauss(N IV])+Gauss(Si IV)+bbodyrad+diskir)`. In this table, Norm refers to the normalization of the associated spectral component, *f* means that the parameter is fixed during the fit, and *p* denotes that the parameter is pegged at its limit. All the unabsorbed fluxes are in units of 10^{-8} erg cm^{-2}s^{-1}. In this model, we fix kT_{uv}, the energy and width of emission lines (described by Gaussian line profiles) at their best-fit values as found in Model 2D. See Section 3.2.3 for more details.

2. The softer Comptonization component ($\Gamma = 1.59 \pm 0.01$, $kT_e = 15.39 \pm 0.35$ keV) dominates the broadband X-ray luminosity, providing ∼50% of the total flux, and gets reflected from a strongly ionized disk ($\xi = 2365.5^{+64.5}_{-46.9}$ erg cm s^{-1}), generating relativistic reflection component. On the other hand, the harder Comptonization component ($\Gamma = 1.17 \pm 0.01$, and $kT_e = 30.6 \pm 1.0$ keV) contributes ∼30% of the total flux and produces unblurred reflection features from a weakly ionized disk ($\xi = 488.1^{+13.8}_{-12.0}$ erg cm s^{-1}), situated far from the ISCO radius.
3. The inner accretion disk is truncated far from the BH, ≃(51–78) R_g and the density of the disk is quite high, $\sim 2 \times 10^{20}$ cm^{-3}.
4. We detect optical/UV emission in excess of the standard multi-temperature blackbody disk emission (see Sections 3.1.2 and 3.1.3, Figures 8 and 9, and Tables 4 and 5 for more details).
5. The UV excess emission is described by a low-temperature blackbody of $kT = 3.27 \pm 0.08$ eV (37, 932 ± 928 K), and three emission lines: Si IV, C IV, and He II (see Figures 6 and 7). Another blackbody component with $kT = 0.80 \pm 0.03$ eV (9200 ± 348 K) accounts for the observed optical excess (see Figure 10).
6. We estimate the reprocessed fraction in the HS by taking a ratio between the 0.1 and 200 keV X-ray flux and the 0.5–10 eV optical/UV flux,[16] and find that 0.9% of the

[16] Since the outer disk can intrinsically emit a significant fraction of optical/UV photons in the 0.5–10.0 eV band through viscous dissipation, we consider only the flux of two `bbodyrad` components and emission lines in that band for computing reprocessed fraction.

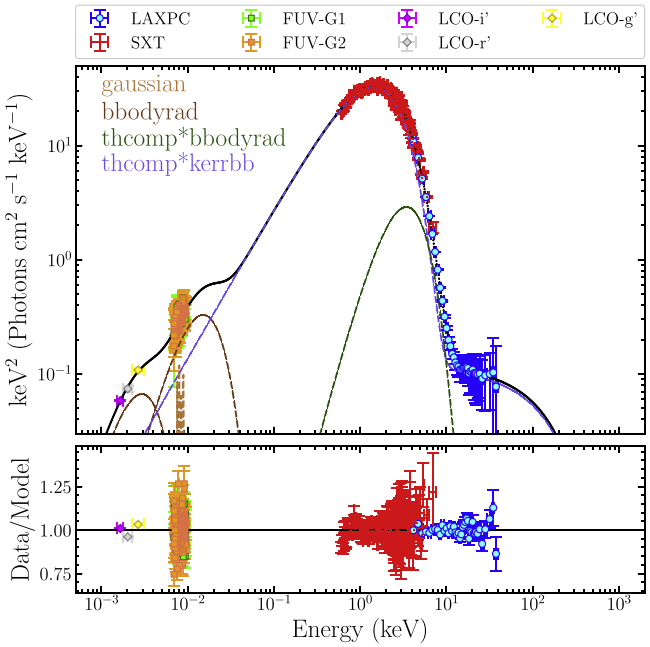

Figure 16. Broadband (optical to hard X-ray) unabsorbed SED (upper panel) and residuals (lower panel), in the form of ratio (data/model), corresponding to Model 2F (SS observation). The total model is represented by a solid black line in the upper panel. Data are rebinned for plotting purposes. See Section 3.2.3 for more details.

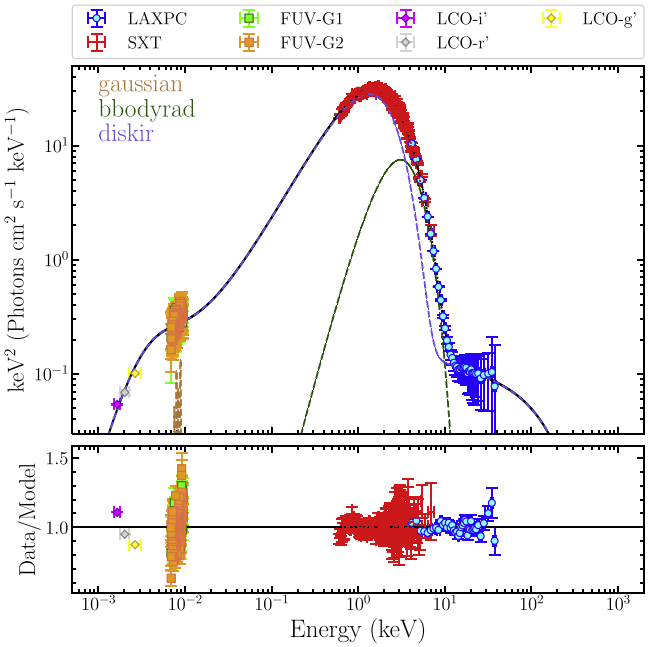

Figure 17. Broadband (optical to hard X-ray) unabsorbed SED (upper panel) and residuals (lower panel), in the form of ratio (data/model), corresponding to Model 2G (SS observation). The total model is represented by a solid black line in the upper panel. Data are rebinned for plotting purposes. See Section 3.2.3 for more details.

bolometric X-ray flux gets reprocessed and thermalized in the outer disk.

During the second AstroSat observation in the SS, the source was found to accrete at an X-ray luminosity of $\sim 1.1 \times 10^{38}$ erg s^{-1} ($\sim$13% of Eddington luminosity, estimated assuming $M = 6.75\,M_{\odot}$). The main results of our multi-wavelength spectral study of the SS can be summarized as follows.

1. The SS X-ray spectrum, in the energy band 0.6–40.0 keV, is comprised of a multi-temperature disk component with $kT_{\rm in} = 0.58 \pm 0.02$ keV, a soft excess, and a weak Comptonization component ($\Gamma = 2.19 \pm 0.05$, and $kT_{\rm e} \gtrsim 36.5$ keV; see Section 3.2.1 and Table 6). The soft X-ray excess, which most likely arises from the plunging region (Fabian et al. 2020), is well described by a blackbody component with $kT = 0.79 \pm 0.02$ keV.
2. Using the continuum fitting method and employing the `kerrbb` model, we measure the BH spin and mass for the source to be $a = 0.85^{+0.10}_{-0.25}$ and $M_{\rm BH} > 5.9\,M_{\odot}$ for an inclination of 64°, which is the jet inclination angle.
3. Similar to the HS case, we detect optical/UV excess components in the SS (see Figures 13 and 14), which is comprised of two low-temperature blackbody components ($kT = 3.87 \pm 0.24$ eV and 0.75 ± 0.04 eV or $kT =$ 44, 892 ± 2784 K and 8704 ± 464 K) and five emission lines: Si IV, N IV], C IV, He II, and N IV (see Sections 3.2.2 and 3.2.3, Figures 11, 12, 15, 16, and 17, and Tables 7 and 8 for more details).
4. The flux in the optical/UV band (0.5–10 eV) is found to be significantly smaller than that of the HS case. Consequently, the reprocessed fraction is low ($\sim 2 \times 10^{-3}$), which is directly estimated by fitting the multi-wavelength data to the irradiated disk model `diskir`. The reprocessed fraction is estimated to be $\sim 3.5 \times 10^{-3}$, from the ratio of flux[16] in the 0.5–10 eV to that in the 0.1–200 keV band. The reduction of optical/UV flux in the SS (compared to the HS) has also been noticed earlier for the BH-LMXB XTE J1817-330 (Gierliński et al. 2009).
5. We estimate the outer disk radius directly from our spectral fitting with the `diskir` model, and find a radius of $(2.30 \pm 0.33) \times 10^{11}$ cm, assuming $i = 64°$.

We discuss below the implications of our multiwavelength spectral results in the HS and SS.

4.1. Inner Accretion Geometry in the HS

The geometry of the inner accretion flow in the HS is the subject of ongoing debate. The current paradigm suggests that the disk truncates far from the ISCO radius in the HS and is replaced by a hot accretion flow (Done et al. 2007). However, this picture has been contested in many works, and an alternative geometry of disk extending into the ISCO radius (or almost ISCO) has emerged (Reis et al. 2010; Kara et al. 2019). For example, Buisson et al. (2019) and Chakraborty et al. (2020) performed a reflection analysis of MAXI J1820 +070 in the HS using data from the NuSTAR mission, and found that the disk has reached almost the ISCO radius ($\sim$2–6 R_g) with their two-component Comptonization model (we have also employed a similar model in our work). Chakraborty et al. (2020) also considered the AstroSat HS observation and obtained results similar to those from their NuSTAR analysis. In both these works, the inclination was low $\sim$30° and the iron abundance high, 4–10 times the solar abundance. Such a high iron abundance is unlikely as the donor star is a low-mass weakly evolved star (Zdziarski et al. 2021a; Mikołajewska et al. 2022). Besides, the binary inclination of the source or the inclination of the jet was estimated to be >59°.

On the other hand, Zdziarski et al. (2021a, 2022b) also performed reflection analyses using the NuSTAR HS data (along with INTEGRAL and Insight-HXMT data in the latter work), some of which were considered in the two previously mentioned works, and found the disk to be truncated far from the ISCO radius with a similar double Comptonization model. A similar conclusion regarding the truncation of the inner accretion disk was reported with NICER, NuSTAR, and SWIFT data using the JED-SAD model in Marino et al. (2021).

Unlike the previous works (Buisson et al. 2019; Chakraborty et al. 2020), both the inclination value ($\gtrsim 50°$) and the iron abundance ($\sim$1–2.6 $A_{\rm Fe}$) in the studies by Zdziarski et al. (2021a, 2022b) do not suffer from the earlier inconsistencies. Their proposed HS geometry consists of two Comptonization components: the harder component having a larger scale height accretion flow located downstream of the truncation radius, and the softer component forming a corona over the inner part of the disk. The harder part is reflected from the remote part of a weakly ionized disk, whereas the softer component gets reflected from a highly ionized underlying disk producing relativistic reflection features. However, the disk temperature ($\sim$0.4–0.5 keV) reported in Zdziarski et al. (2022b) is significantly higher than the inner disk temperature obtained with the NICER data (Wang et al. 2020). Finally, in all the above works, the low-energy data (<2.0 keV) were not used to perform the analysis, and only constant density reflection models, i.e., density ($n_{\rm e}$) is fixed to $10^{15}\,{\rm cm}^{-3}$, (like `relxilllpCp`, `reflkerr`, `xillverCp`) were employed.

In our work, we include low-energy X-ray data from NICER and AstroSat/SXT down to 0.6 keV to obtain a robust picture of the accretion geometry in the HS. This approach is not only helpful in consistently constraining the disk components but also in providing a clearer picture of the inner accretion flow (García et al. 2015). The HS spectra in the 0.6–150 keV band are well described by a structured accretion flow consisting of two Comptonization components (see Section 3.1.1 and Table 3 for more details). The softer component is found to dominate the broadband X-ray luminosity, and is reflected from a strongly ionized disk, producing the relativistic reflection features. The inner disk responsible for the relativistic reflection is truncated far from the source, $\simeq$51–78 R_g. We calculate a reflection fraction of $\sim$0.25 for this component as the ratio of the reflected flux in the 1 eV–1000 keV band (the reflected spectrum of `reflionxhd` is calculated over this energy range) to the incident flux in the 0.1–1000 keV band (Fürst et al. 2015). The harder component is reflected from a further distant and moderately ionized disk. The corresponding reflection fraction is $\sim$0.13. One should note that the definition of reflection fraction we use differs from that of Dauser et al. (2016). Since the softer component has higher Γ and lower $kT_{\rm e}$ than the harder component, it is most likely located closer to the accretion disk (Haardt & Maraschi 1991). The relatively higher values of the reflection fraction and the ionization parameter also support this picture. Besides, a hard Comptonized spectrum of $\Gamma \sim 1.2$ implies that the hot Comptonizing plasma is situated away from the disk (Poutanen et al. 2018). Furthermore, the section of the disk reflecting the harder Comptonized component exhibits moderate ionization. This suggests that the scale height of the accretion flow emitting the harder Comptonization component is likely large. Therefore, our investigation broadly aligns with the accretion geometry of this source as described by Zdziarski et al. (2021a) (please refer to their Sections 3 and 4 for more detailed information on the geometry). The spectral parameters, such as the power-law index and electron temperature, associated with the two Comptonization components are close to those reported in Zdziarski et al. (2022b) for the nearest NuSTAR observation (their epoch 1 observation, which was performed approximately 6 days prior to our HS observation). However, there are differences in the values of the reflection parameters between our work and theirs. This discrepancy may be related to the fact that we consider the possibility of a higher-density disk. Specifically, we leave the parameter log ($n_{\rm e}$) free during the spectral fitting, whereas it was fixed to a default value of $n_{\rm e} = 10^{15}\,{\rm cm}^{-3}$ in all the other works.

It was previously suggested that a higher value of disk density can influence the thermodynamic processes in the reflection skin of the disk, i.e., the disk atmosphere. At higher densities, free–free heating becomes more dominant, leading to an increase in the temperature of the disk atmosphere. This, in turn, results in a soft excess below 2 keV in a disk with higher density (García et al. 2016). Furthermore, a soft excess in a higher-density disk may also arise because ionization parameters fitted at different densities are of a similar order. This results in a higher irradiating X-ray flux for a disk with higher density (see Zdziarski & De Marco 2020 for more details). Therefore, the impact of a higher-density disk on the X-ray spectra can be better understood when including low-energy data (<2.0 keV). To investigate how a higher density disk could affect the spectral parameters, we fix the density to $10^{15}\,{\rm cm}^{-3}$ in our Model 1A, and fit the model to the data. This results in a relatively poor fit with a χ^2/dof of 2574.1/2389 ($\Delta\chi^2 = +669.9$ for one less parameter). Additionally, we observe significant changes in the values of the ionization parameter, iron abundance, and the radius of the inner disk, consistent with earlier findings in Tomsick et al. (2018) and Chakraborty et al. (2021). The iron abundance increases to the maximum allowed value of 5. The ionization parameter associated with the reflection of the harder Comptonization component got pegged to 0, while it increased to a much higher value (around $\sim$4000) for the reflection of the softer Comptonization component compared to the case with a free log ($n_{\rm e}$). Furthermore, the inner disk radius ($\mathcal{R}_{\rm in}$) becomes poorly constrained in this model, with $\mathcal{R}_{\rm in} > 110 R_g$. Thus, both the physical consistency of the best-fit parameters and the statistical significance of the spectral fit indicate a higher-density disk in MAXI J1820+070. However, as emphasized in García et al. (2016), the atomic physics considered in these reflection models is uncertain beyond $10^{19}{\rm cm}^{-3}$. Thus, more accurate determination of the rates of the pertinent atomic processes at higher densities could influence the spectrum of these reflection models, thereby our results also may be affected.

4.2. Mass and Spin of MAXI J1820+070

We constrain the BH spin and mass by fitting the `kerrbb` model to the SS X-ray spectrum of MAXI J1820+070. This method requires the emission to be disk dominated where the disk (in general) reaches the ISCO and it remains thin. These two requirements are thought to be met when the disk fraction $\geqslant$75% (substantial thermal component) and $L/L_{\rm Edd} < 0.3$ (the disk scale height grows beyond this, and the thin disk model may not hold) (McClintock et al. 2014). We find the disk fraction to be $\sim$85% and $L/L_{\rm Edd} \sim 0.13$ in the SS of

MAXI J1820+070 using Model 2A, thus making our SS X-ray spectrum suitable for the estimation of BH spin and mass.

Additionally, a meaningful estimation of the BH mass and spin requires proper knowledge of the distance to the source and the inclination of the inner disk. While the distance to the source is well measured to be 2.96 ± 0.33 kpc, the inclination is less certain (see the introduction section for more details). Besides, the outer disk could be misaligned with respect to the BH spin axis (Poutanen et al. 2022), which further complicates the estimation of inclination. However, the inclination of the inner disk is most likely the same as the jet inclination of $64° \pm 5°$ (which can be considered to be aligned with the BH spin axis) as measured by Wood et al. (2021). If we fix the inclination parameter to 64°, we obtain the BH spin, $a = 0.85^{+0.10}_{-0.25}$ and mass, $M_{\rm BH} > 5.9 M_{\odot}$ (see Table 6 and Section 3.2.1 for further details). Our spin measurement agrees well with the estimation of Bhargava et al. (2021) ($a = 0.799^{+0.016}_{-0.015}$) based on an independent timing-based technique utilizing the evolution of the characteristic frequencies in the power density spectra. Furthermore, the BH mass we find is consistent with that measured by Torres et al. (2020) ($M_{\rm BH} = 5.73$–$8.34\, M_{\odot}$ for binary inclination in the range of 66°–81°, with a 95% confidence level). A recent determination of mass (Mikołajewska et al. 2022) of this system ($M = 6.75^{+0.64}_{-0.46} M_{\odot}$ with a 68% confidence level) is also in line with our estimation. By constraining the inclination parameter in the range of 59°–69° and mass in the range of 5.0–10.0 $M_{\odot}$ in the `kerrbb` model, we measure the BH spin to be $a = 0.77 \pm 0.21$.

4.3. X-Ray Irradiation and Geometry of the Outer Disk

It is widely believed that the reprocessing of X-rays in the outer disk plays a dominant role in the optical/UV emission in BH-LMXBs (van Paradijs & McClintock 1994; Gierliński et al. 2009). In the case of MAXI J1820+070, we find clear evidence of reprocessed emission in terms of excess optical/UV continuum and strong emission lines. To describe the optical/UV excess components phenomenologically, we require two low-temperature blackbody components, suggesting reprocessed emission from a range of radii rather than a narrow annulus of the disk. Furthermore, we find that the multiwavelength spectral fit with the irradiated disk model `diskir` provides a significantly worse fit than our phenomenological models with two low-temperature blackbody components. This is perhaps not unexpected as the `diskir` model assumes uniform illumination of the outer accretion disk by the inner accretion flow, captured through the constant $f_{\rm out}$. In this context, we calculate the ratio of two single-temperature blackbody fluxes (representing UV and optical excesses, respectively) in the energy band 0.5–10.0 eV to the incoming X-ray flux in the energy band 0.1–200.0 keV in the HS and SS, and find this to be different, suggesting a non-uniform illumination of the outer accretion disk. In the HS, the ratio of UV excess flux (0.5–10 eV) and the X-ray flux (0.1–200.0 keV) is $\sim 5.8 \times 10^{-3}$, and the ratio of optical excess flux (0.5–10 eV) and the X-ray flux (0.1–200.0 keV) is $\sim 3.2 \times 10^{-3}$ (Model 1C is used for this estimation). On the other hand, the same quantities in the SS are $\sim 2 \times 10^{-3}$ and $\sim 1.3 \times 10^{-3}$, respectively (Model 2E is employed for this calculation). Generally, $f_{\rm out}$ should be a function of the disk aspect ratio, H/R (H is the disk scale height and R is the radius) and H/R itself depends on R (Frank et al. 2002; Meshcheryakov et al. 2018). However, in `diskir`, H/R is assumed to be constant, which is a limiting case in the actual scenario (Meshcheryakov et al. 2018). For example, $H \propto R^{9/8}$ in the outer zone of the standard Shakura–Sunyaev model, whereas $H \propto R^{9/7}$ in the isothermal disk model of Cunningham (Kimura & Done 2019).

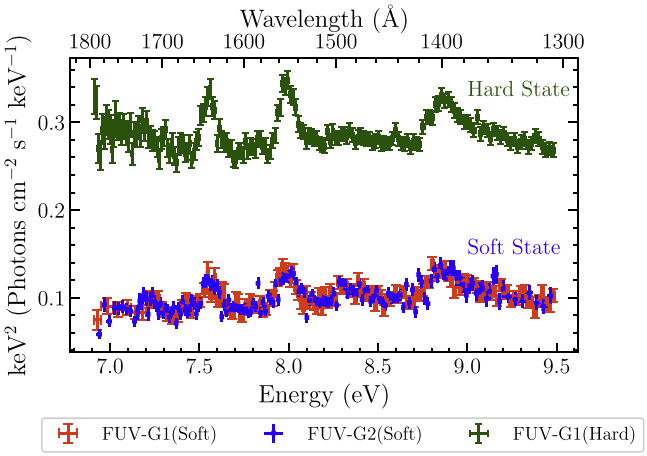

Figure 18. HS and SS unfolded FUV spectra. The models 1B (HS) and 2D (SS) are used for this purpose. See Sections 3.1.2 and 3.2.2 for more details.

The observed optical/UV flux in the 0.5–10 eV band, calculated from our multiwavelength spectra, is ∼4 and ∼33 times higher than those estimated for the intrinsic disk emission in the SS and HS using the models 2E and 1C, respectively. This clearly implies the dominance of X-ray irradiation over the intrinsic viscous dissipation in the outer disk in both the SS and HS. We find that the strength of the reprocessed optical/UV emission relative to the intrinsic disk emission is much higher in the HS than that in the SS. This is also evident from the stronger FUV grating spectrum in the HS, as can be observed in Figure 18. Also, the fraction of the intrinsic disk/corona emission reprocessed in the disk is nearly a factor of 3 higher in the HS ($\sim 9 \times 10^{-3}$) than in the SS ($\sim 3.5 \times 10^{-3}$). These observations clearly demonstrate that X-ray irradiation onto the disk is much more dominant in the HS of MAXI J1820+070, similar to that found in BH-LMXB XTE J1817-330 (Gierliński et al. 2009). The stronger optical and possibly UV continuum in the HS, in principle, could also arise due to the synchrotron emission from jets (Russell et al. 2006). The SED and timing studies of MAXI J1820+070 have shown that the jet does make a contribution to the infrared band and to the optical band to some extent (Paice et al. 2019; Markoff et al. 2020; Zdziarski et al. 2022a). However, we find that the stronger FUV continuum is accompanied by strong emission lines in the HS. The emission lines due to He II, C IV, and Si IV are nearly a factor of 2 stronger in the HS than in the SS, implying that most of the excess UV/optical emission in the HS is due to X-ray reprocessing in the outer accretion disk. The stronger X-ray reprocessing in the HS is most likely the outcome of the geometry where the X-ray corona in the innermost regions has a larger scale height than the accretion disk, possibly in the form of a spherical corona or elongated along the jet axis. In addition, the disk wind, observed during the HS (Muñoz-Darias et al. 2019), can also contribute to the irradiation of the disk, increasing the optical/UV flux (Gierliński et al. 2009; Dubus et al. 2019; Tetarenko et al. 2020).

We also note that it is unlikely that the emission from the secondary star is contributing a significant number of photons

to the optical/UV band in both states, as the surface temperature is low, ∼4200 K, i.e., ∼0.36 eV (Mikołajewska et al. 2022), which is much lower than the temperature of the blackbody (∼0.8 eV). However, the companion, which is detected in the optical only during quiescence, is fainter than the observed fluxes in outburst.

Finally, the high observed reprocessed fraction ($\sim 10^{-2}$–10^{-3}) from MAXI J1820+070 is unlikely to be achieved in the framework of the standard thin disk prescription (Dubus et al. 1999). The outer disk is most likely convex or warped in shape, making the disk more effective for X-ray reprocessing. Interestingly, Thomas et al. (2022) proposed the outer disk of MAXI J1820+070 to be warped to explain the large amplitude modulation seen in the HS optical light curves. Furthermore, a significant spin–orbit misalignment has been inferred from the optical polarimetric observations of this source (Poutanen et al. 2022), which could also result in a warped accretion disk.

5. Conclusion

Utilizing data from the AstroSat, NICER, and LCO observatories, we constrain the inner and outer geometries of the accretion flow around the BH-LMXB MAXI J1820+070 in the HS and SS during its 2018 outburst. In the HS, our analysis reveals that the inner accretion disk is truncated far from the ISCO radius, and has been replaced by a structured accretion flow containing two Comptonization components with different slopes and temperatures. The softer Comptonization component dominates the X-ray emission and produces broad relativistic X-ray reflection features. Meanwhile, the harder component undergoes reflection from a distant, high-density disk ($\sim 2 \times 10^{20}\,\mathrm{cm}^{-3}$), resulting in unblurred reflection features. In the SS, the X-ray spectrum features a dominant disk component (disk fraction ∼85%), a soft X-ray excess, and a weak Comptonization component. We estimate the spin of BH using the continuum spectral fitting method, yielding $a = 0.77 \pm 0.21$, for an inclination in the range of 59°–69° (i.e., the range of jet inclination angle) and a mass in the range of 5.0–10.0 $M_{\odot}$ (predicted mass range of this BH). Finally, we find that a significant fraction of the X-ray radiation from the inner disk and the coronal emission is reprocessed and thermalized in the outer accretion disk, with the reprocessed fraction being much higher in the HS ($\sim 9 \times 10^{-3}$) compared to the SS ($\sim 3.5 \times 10^{-3}$). A strong reprocessing in the outer accretion disk likely suggests that the outer disk could be warped or convex, as also indicated in Thomas et al. (2022).

Acknowledgments

We thank the anonymous referee for his/her constructive comments that helped to improve the manuscript. We use data from the AstroSat mission of the Indian Space Research Organization (ISRO), archived at the Indian Space Science Data Center (ISSDC). We acknowledge the POC teams of the SXT, LAXPC, CZTI, and UVIT instruments for archiving data and providing the necessary software tools. This research has made use of data and software provided by the High Energy Astrophysics Science Archive Research Center (HEASARC), which is a service of the Astrophysics Science Division at NASA/GSFC. We acknowledge the use of MAXI data provided by RIKEN, JAXA, and the MAXI team, and of public data from the NICER data archive. This work also uses data from the Faulkes Telescope Project, which is an education partner of LCO. The Faulkes Telescopes are maintained and operated by LCO. A.A.Z. acknowledges support from the Polish National Science Center under grant No. 2019/35/B/ST9/03944. We would like to express our gratitude to John Tomsick for providing the `reflionxhd` model, and we extend our thanks to Michael Parker for developing this model. S.B. also wants to acknowledge the valuable assistance provided by Sudip Chakraborty, Nilam Navale, and Labanya K. Guha in the preparation of this manuscript.

ORCID iDs

Srimanta Banerjee https://orcid.org/0000-0002-6051-6928
Gulab C. Dewangan https://orcid.org/0000-0003-1589-2075
Poshak Gandhi https://orcid.org/0000-0003-3105-2615
N. P. S. Mithun https://orcid.org/0000-0003-3431-6110
Payaswini Saikia https://orcid.org/0000-0002-5319-6620
Dipankar Bhattacharya https://orcid.org/0000-0003-3352-3142
David M. Russell https://orcid.org/0000-0002-3500-631X
Fraser Lewis https://orcid.org/0000-0003-3352-2334
Andrzej A. Zdziarski https://orcid.org/0000-0002-0333-2452

References

Antia, H. M., Agrawal, P. C., Dedhia, D., et al. 2021, JApA, 42, 32
Antia, H. M., Yadav, J. S., Agrawal, P. C., et al. 2017, ApJS, 231, 10
Arnaud, K. A. 1996, in ASP Conf. Ser. 101, Astronomical Data Analysis Software and Systems V, ed. G. H. Jacoby & J. Barnes (San Francisco, CA: ASP), 17
Atri, P., Miller-Jones, J. C. A., Bahramian, A., et al. 2020, MNRAS, 493, L81
Axelsson, M., & Veledina, A. 2021, MNRAS, 507, 2744
Baglio, M. C., Russell, D. M., & Lewis, F. 2018, ATel1, 11418, 1
Bahramian, A., Strader, J., & Dage, K. 2018, ATel1, 11424, 1
Banerjee, S., Chakraborty, C., & Bhattacharyya, S. 2019a, ApJ, 870, 95
Banerjee, S., Chakraborty, C., & Bhattacharyya, S. 2019b, MNRAS, 487, 3488
Banerjee, S., Gilfanov, M., Bhattacharyya, S., & Sunyaev, R. 2020, MNRAS, 498, 5353
Basak, R., & Zdziarski, A. A. 2016, MNRAS, 458, 2199
Belloni, T. M. 2010, The Jet Paradigm, Lecture Notes in Physics, vol. 794 (Berlin: Springer), 53
Belloni, T. M., & Motta, S. E. 2016, in Astrophysics of Black Holes, Astrophysics and Space Science Library, ed. C. Bambi, vol. 440 (Berlin: Springer), 61
Bhalerao, V., Bhattacharya, D., Vibhute, A., et al. 2017, JApA, 38, 31
Bhargava, Y., Belloni, T., Bhattacharya, D., Motta, S., & Ponti, G. 2021, MNRAS, 508, 3104
Bright, J., Fender, R., & Motta, S. 2018, ATel1, 11420, 1
Bright, J. S., Fender, R. P., Motta, S. E., et al. 2020, NatAs, 4, 697
Buisson, D. J. K., Fabian, A. C., Barret, D., et al. 2019, MNRAS, 490, 1350
Casella, P., Vincentelli, F., O'Brien, K., et al. 2018, ATel1, 11451, 1
Chakraborty, S., Navale, N., Ratheesh, A., & Bhattacharyya, S. 2020, MNRAS, 498, 5873
Chakraborty, S., Ratheesh, A., Bhattacharyya, S., et al. 2021, MNRAS, 508, 475
Connors, R. M. T., García, J. A., Tomsick, J., et al. 2021, ApJ, 909, 146
Dauser, T., Garcia, J., Parker, M. L., Fabian, A. C., & Wilms, J. 2014, MNRAS, 444, L100
Dauser, T., García, J., Walton, D. J., et al. 2016, A&A, 590, A76
Dauser, T., Wilms, J., Reynolds, C. S., & Brenneman, L. W. 2010, MNRAS, 409, 1534
De Marco, B., Zdziarski, A. A., Ponti, G., et al. 2021, A&A, 654, A14
Denisenko, D. 2018, ATel1, 11400, 1
Dewangan, G. C. 2021, JApA, 42, 49
Done, C., Gierliński, M., & Kubota, A. 2007, A&ARv, 15, 1
Dubus, G., Done, C., Tetarenko, B. E., & Hameury, J.-M. 2019, A&A, 632, A40
Dubus, G., Lasota, J.-P., Hameury, J.-M., & Charles, P. 1999, MNRAS, 303, 139

Dzielak, M. A., De Marco, B., & Zdziarski, A. A. 2021, MNRAS, 506, 2020
Echiburú-Trujillo, C., Tetarenko, A. J., Haggard, D., et al. 2024, ApJ, 962, 116
Fabian, A. C. 2005, in Broad iron lines in AGN and X-ray binaries, ed. T. J. Maccarone, R. P. Fender, & L. C. Ho (Dordrecht: Springer), 97
Fabian, A. C., Buisson, D. J., Kosec, P., et al. 2020, MNRAS, 493, 5389
Fabian, A. C., Rees, M. J., Stella, L., & White, N. E. 1989, MNRAS, 238, 729
Frank, J., King, A., & Raine, D. J. 2002, Accretion Power in Astrophysics (3rd ed.; Cambridge: Cambridge Univ. Press)
Fürst, F., Nowak, M. A., Tomsick, J. A., et al. 2015, ApJ, 808, 122
Gandhi, P., Paice, J. A., Littlefair, S. P., et al. 2018, ATel1, 11437, 1
García, J., Dauser, T., Lohfink, A., et al. 2014, ApJ, 782, 76
García, J., Dauser, T., Reynolds, C. S., et al. 2013, ApJ, 768, 146
García, J. A., Dauser, T., Steiner, J. F., et al. 2015, ApJL, 808, L37
García, J. A., Fabian, A. C., Kallman, T. R., et al. 2016, MNRAS, 462, 751
Gendreau, K. C., Arzoumanian, Z., Adkins, P. W., et al. 2016, Proc. SPIE, 9905, 99051H
Gierliński, M., Done, C., & Page, K. 2009, MNRAS, 392, 1106
Gilfanov, M. 2010, in Lecture Notes in Physics, ed. T. Belloni, 794 (Berlin: Springer), 17
Gilfanov, M., & Arefiev, V. 2005, arXiv:astro-ph/0501215
Haardt, F., & Maraschi, L. 1991, ApJL, 380, L51
Harris, D. W., Jensen, T. W., Suzuki, N., et al. 2016, AJ, 151, 155
HI4PI Collaboration, Ben Bekhti, N., Flöer, L., et al. 2016, A&A, 594, A116
Homan, J., & Belloni, T. 2005, Ap&SS, 300, 107
Homan, J., Bright, J., Motta, S. E., et al. 2020, ApJL, 891, L29
Homan, J., Stevens, A. L., Altamirano, D., et al. 2018, ATel1, 12068, 1
Homan, J., Wijnands, R., van der Klis, M., et al. 2001, ApJS, 132, 377
Jiang, J., Gallo, L. C., Fabian, A. C., Parker, M. L., & Reynolds, C. S. 2020, MNRAS, 498, 3888
Kaastra, J. S., & Bleeker, J. A. M. 2016, A&A, 587, A151
Kajava, J. J. E., Motta, S. E., Sanna, A., et al. 2019, MNRAS, 488, L18
Kara, E., Steiner, J. F., Fabian, A. C., et al. 2019, Natur, 565, 198
Kawamuro, T., Negoro, H., Yoneyama, T., et al. 2018, ATel1, 11399, 1
Kimura, M., & Done, C. 2019, MNRAS, 482, 626
Kubota, A., Tanaka, Y., Makishima, K., et al. 1998, PASJ, 50, 667
Kumar, S., Dewangan, G. C., Singh, K. P., et al. 2023, ApJ, 950, 90
Lewis, F. 2018, RTSRE, 1, 237
Li, L.-X., Zimmerman, E. R., Narayan, R., & McClintock, J. E. 2005, ApJS, 157, 335
Liska, M., Hesp, C., Tchekhovskoy, A., et al. 2018, MNRAS, 474, L81
Littlefield, C. 2018, ATel1, 11421, 1
Makishima, K., Maejima, Y., Mitsuda, K., et al. 1986, ApJ, 308, 635
Mandal, A. K., Singh, A., Stalin, C. S., Chandra, S., & Gandhi, P. 2018, ATel1, 11458, 1
Marino, A., Barnier, S., Petrucci, P. O., et al. 2021, A&A, 656, A63
Markoff, S., Russell, D. M., Dexter, J., et al. 2020, MNRAS, 495, 525
McClintock, J. E., Narayan, R., & Steiner, J. F. 2014, SSRv, 183, 295
Meshcheryakov, A. V., Tsygankov, S. S., Khamitov, I. M., et al. 2018, MNRAS, 473, 3987
Mikołajewska, J., Zdziarski, A. A., Ziółkowski, J., Torres, M. A. P., & Casares, J. 2022, ApJ, 930, 9
Mitsuda, K., Inoue, H., Koyama, K., et al. 1984, PASJ, 36, 741
Morton, D. C. 2003, ApJS, 149, 205
Muñoz-Darias, T., Jiménez-Ibarra, F., Panizo-Espinar, G., et al. 2019, ApJL, 879, L4
Özbey Arabacı, M., Kalemci, E., Dinçer, T., et al. 2022, MNRAS, 514, 3894
Paice, J. A., Gandhi, P., Shahbaz, T., et al. 2019, MNRAS, 490, L62
Pirbhoy, S. F., Baglio, M. C., Russell, D. M., et al. 2020, ATel1, 13451, 1
Postma, J. E., & Leahy, D. 2017, PASP, 129, 115002
Poutanen, J., Veledina, A., Berdyugin, A. V., et al. 2022, Sci, 375, 874
Poutanen, J., Veledina, A., & Zdziarski, A. A. 2018, A&A, 614, A79
Reis, R. C., Fabian, A. C., & Miller, J. M. 2010, MNRAS, 402, 836
Reis, R. C., Miller, J. M., & Fabian, A. C. 2009, MNRAS, 395, L52
Remillard, R. A., Loewenstein, M., Steiner, J. F., et al. 2021, arXiv:2105.09901
Remillard, R. A., & McClintock, J. E. 2006, ARA&A, 44, 49
Rodi, J., Tramacere, A., Onori, F., et al. 2021, ApJ, 910, 21
Ross, R. R., & Fabian, A. C. 2005, MNRAS, 358, 211
Ross, R. R., & Fabian, A. C. 2007, MNRAS, 381, 1697
Russell, D. M., Baglio, M. C., & Lewis, F. 2019a, ATel1, 12534, 1
Russell, D. M., Bramich, D. M., Lewis, F., et al. 2019b, AN, 340, 278
Russell, D. M., Fender, R. P., Hynes, R. I., et al. 2006, MNRAS, 371, 1334
Sako, S., Ohsawa, R., Ichiki, M., et al. 2018, ATel1, 11426, 1
Shakura, N. I., & Sunyaev, R. A. 1973, A&A, 24, 337
Shidatsu, M., Nakahira, S., Murata, K. L., et al. 2019, ApJ, 874, 183
Shimura, T., & Takahara, F. 1995, ApJ, 445, 780
Singh, K., Stewart, G., Westergaard, N., et al. 2017, JApA, 38, 29
Singh, K. P., Stewart, G. C., Chandra, S., et al. 2016, Proc. SPIE, 9905, 99051E
Singh, K. P., Tandon, S. N., Agrawal, P. C., et al. 2014, Proc. SPIE, 9144, 91441S
Sunyaev, R. A., & Titarchuk, L. G. 1980, A&A, 86, 121
Tandon, S., Postma, J., Joseph, P., et al. 2020, AJ, 159, 158
Tandon, S., Subramaniam, A., Girish, V., et al. 2017, AJ, 154, 128
Tetarenko, B. E., Dubus, G., Marcel, G., Done, C., & Clavel, M. 2020, MNRAS, 495, 3666
Thomas, J. K., Charles, P. A., Buckley, D. A. H., et al. 2022, MNRAS, 509, 1062
Tomsick, J. A., Parker, M. L., García, J. A., et al. 2018, ApJ, 855, 3
Tonry, J. L., Denneau, L., Flewelling, H., et al. 2018, ApJ, 867, 105
Torres, M. A. P., Casares, J., Jiménez-Ibarra, F., et al. 2019, ApJL, 882, L21
Torres, M. A. P., Casares, J., Jiménez-Ibarra, F., et al. 2020, ApJL, 893, L37
Trushkin, S. A., Nizhelskij, N. A., Tsybulev, P. G., & Erkenov, A. 2018, ATel1, 11439, 1
Uttley, P., Gendreau, K., Markwardt, C., et al. 2018, ATel1, 11423, 1
Vadawale, S. V., Rao, A. R., Bhattacharya, D., et al. 2016, Proc. SPIE, 9905, 99051G
van Paradijs, J., & McClintock, J. E. 1994, A&A, 290, 133
Vanden Berk, D. E., Richards, G. T., Bauer, A., et al. 2001, AJ, 122, 549
Verner, D. A., Ferland, G. J., Korista, K. T., & Yakovlev, D. G. 1996, ApJ, 465, 487
Wang, Y., Ji, L., Zhang, S. N., et al. 2020, ApJ, 896, 33
Weisskopf, M. C., Guainazzi, M., Jahoda, K., et al. 2010, ApJ, 713, 912
Wilms, J., Allen, A., & McCray, R. 2000, ApJ, 542, 914
Wood, C. M., Miller-Jones, J. C. A., Homan, J., et al. 2021, MNRAS, 505, 3393
Yadav, J., Agrawal, P., Antia, H., et al. 2016, Proc. SPIE, 9905, 99051D
Zdziarski, A. A., & De Marco, B. 2020, ApJL, 896, L36
Zdziarski, A. A., Dzielak, M. A., De Marco, B., Szanecki, M., & Niedźwiecki, A. 2021a, ApJL, 909, L9
Zdziarski, A. A., Jourdain, E., Lubiński, P., et al. 2021b, ApJL, 914, L5
Zdziarski, A. A., Johnson, W. N., & Magdziarz, P. 1996, MNRAS, 283, 193
Zdziarski, A. A., Szanecki, M., Poutanen, J., Gierliński, M., & Biernacki, P. 2020, MNRAS, 492, 5234
Zdziarski, A. A., Tetarenko, A. J., & Sikora, M. 2022a, ApJ, 925, 189
Zdziarski, A. A., You, B., Szanecki, M., Li, X.-B., & Ge, M. 2022b, ApJ, 928, 11
Zhang, L., Altamirano, D., Cúneo, V. A., et al. 2020, MNRAS, 499, 851
Zhao, X., Gou, L., Dong, Y., et al. 2021, ApJ, 916, 108
Zhu, H., Tian, W., Li, A., & Zhang, M. 2017, MNRAS, 471, 3494
Życki, P. T., Done, C., & Smith, D. A. 1999, MNRAS, 309, 561